Cell Metabolism

Article

Defects in a liver-bone axis contribute to hepatic osteodystrophy disease progression

Graphical abstract

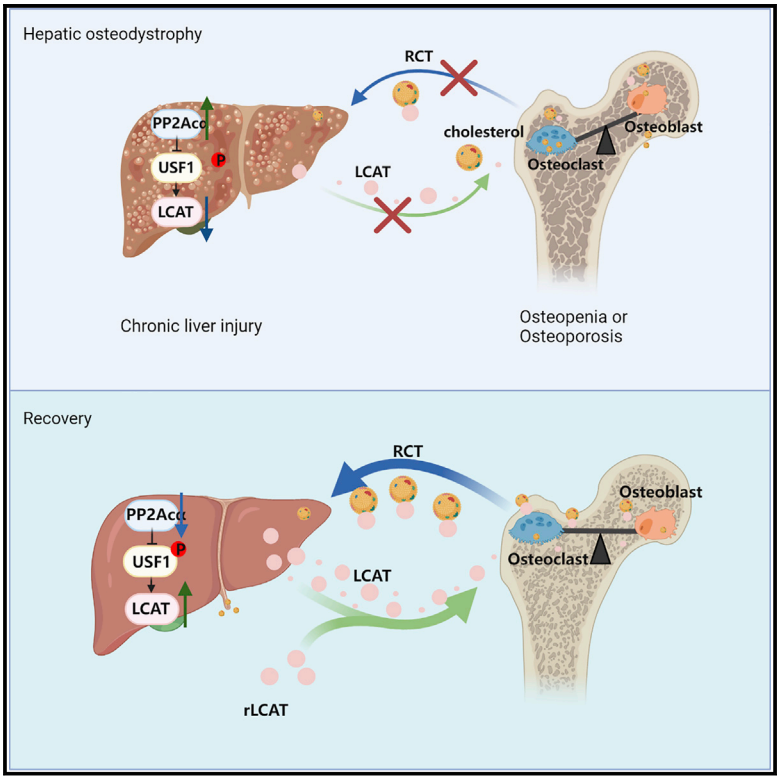

Highlights

- High levels of PP2Acα in the liver correlate with bone loss in individuals with HOD
- Upregulation of LCAT expression in the liver ameliorates bone loss in HOD mice
- PP2Acα downregulates LCAT expression through dephosphorylation of USF1
- LCAT improves liver function by reversing cholesterol transport from bone to liver

Authors

Ke Lu, Tian-Shu Shi, Si-Yu Shen, ..., Chao-Jun Li, Bin Xue, Qing Jiang

Correspondence

di.chen@siat.ac.cn (D.C.),
licj@nicemice.cn (C.-J.L.),
xuebin@njmu.edu.cn (B.X.),
qingj@nju.edu.cn (Q.J.)

In brief

Hepatic osteodystrophy (HOD) is a metabolic bone disease caused by chronic liver injuries. Lu et al. discovered a novel liver-bone axis in the pathogenesis of HOD involving the upregulation of hepatic PP2Acα that leads to reduced expression of the hepatokine lecithin-cholesterol acyltransferase (LCAT) and defects in reverse cholesterol transport from the bone to the liver.

Lu et al., 2022, Cell Metabolism *34*, 441–457
March 1, 2022
https://doi.org/10.1016/j.cmet.2022.02.006

CellPress

Cell Metabolism

CellPress

Article

Defects in a liver-bone axis contribute to hepatic osteodystrophy disease progression

Ke Lu,[1,3,4,10] Tian-Shu Shi,[1,3,10] Si-Yu Shen,[1,3] Yong Shi,[1,3] Hong-Liang Gao,[2] Jing Wu,[2] Xiang Lu,[2] Xiang Gao,[7] Huang-xian Ju,[8] Wei Wang,[9] Yi Cao,[9] Di Chen,[4,*] Chao-Jun Li,[5,6,*] Bin Xue,[2,*] and Qing Jiang[1,3,11,*]

[1]State Key Laboratory of Pharmaceutical Biotechnology, Department of Sports Medicine and Adult Reconstructive Surgery, Nanjing Drum Tower Hospital, The Affiliated Hospital of Nanjing University Medical School, 321 Zhongshan Road, Nanjing 210008, China

[2]Core Laboratory, Sir Run Run Hospital, Nanjing Medical University, Nanjing 211166, China

[3]Branch of National Clinical Research Center for Orthopedics, Sports Medicine and Rehabilitation, 321 Zhongshan Road, Nanjing 210008, China

[4]Faculty of Pharmaceutical Sciences, Shenzhen Institute of Advanced Technology, Chinese Academy of Sciences, Shenzhen 518055, China

[5]Ministry of Education Key Laboratory of Model Animal for Disease Study, Model Animal Research Center of the Medical School, Nanjing University, Nanjing 210093, China

[6]State Key Laboratory of Reproductive Medicine and China International Joint Research Center on Environment and Human Health, Center for Global Health, School of Public Health, Nanjing Medical University, Nanjing 211166, China

[7]Model Animal Research Center of Nanjing University, Xuefu Road, Nanjing 210032, China

[8]State Key Laboratory of Analytical Chemistry for Life Science, Nanjing University, Nanjing 210023, China

[9]National Laboratory of Solid-State Microstructures, Department of Physics, Nanjing University, Nanjing 210093, China

[10]These authors contributed equally

[11]Lead contact

*Correspondence: di.chen@siat.ac.cn (D.C.), licj@nicemice.cn (C.-J.L.), xuebin@njmu.edu.cn (B.X.), qingj@nju.edu.cn (Q.J.)

https://doi.org/10.1016/j.cmet.2022.02.006

SUMMARY

Hepatic osteodystrophy (HOD) is a metabolic bone disease that is often associated with chronic liver disease and is marked by bone loss. Here, we demonstrate that hepatic expression of the phosphatase PP2Acα is upregulated during HOD, leading to the downregulation of expression of the hepatokine lecithin-cholesterol acyltransferase (LCAT). Loss of LCAT function markedly exacerbates the bone loss phenotype of HOD in mice. In addition, we found that alterations in cholesterol levels are involved in the regulation of osteoblast and osteoclast activities. We also found that LCAT improves liver function and relieves liver fibrosis in the mouse HOD model by promoting reversal of cholesterol transport from the bone to the liver. In summary, defects in a liver-bone axis occur during HOD that can be targeted to ameliorate disease progression.

INTRODUCTION

Metabolic stability is important for maintaining proper body homeostasis. The liver, acting as a metabolic center, plays a critical role in this process by interacting with multiple organs to modulate body homeostasis. For example, the liver regulates the function of the intestines and the brain to maintain whole-body energy and ion metabolism by secreting hepcidin, FGF21, and bile acid, among other agents, to form the hepatic-intestinal axis and the hepatic-brain axis (Darshan and Anderson, 2007; Hamoud et al., 2018; Liang et al., 2014; Wang et al., 2008). The regulation of these tissue axes coordinates whole-body metabolic homeostasis and often go awry under pathological conditions.

Another important metabolic organ is the bone, which has been shown to have an important endocrine function (Han et al., 2018). The bone affects glycolipid metabolism, cardiovascular function, and dietary intake and regulates the normal physiological functions of other organs by secreting osteocalcin, sclerostin, lipocalin 2, and other bone-derived factors (Kim et al., 2017; Mosialou et al., 2017; Su et al., 2019). The elevated sclerostin derived from osteocytes correlated with markers of liver dysfunction such as albumin in cirrhosis patients (Rhee et al., 2014). But other organs impinge on the bone. For example, liver-secreted vitamin B12 (VitB12)-derived taurine regulates skeletal development (Roman-Garcia et al., 2014). Likewise, hepatocyte-derived IGFBP1 can increase the transcriptional activity of NFATc1 in osteoclasts, thus affecting bone resorption, by binding to integrin β1 on the surface of osteoclasts (Wang et al., 2015). Therefore, a signaling axis between the liver and the bone exists that regulates their respective functions.

Hepatic osteodystrophy (HOD) is a metabolic bone disease associated with chronic liver disease, such as primary biliary cirrhosis and primary sclerosing cholangitis, and is often marked by osteopenia or osteoporosis (López-Larramona et al., 2011). In particular, HOD affects more than 844 million people worldwide (Shergill et al., 2018), and almost 75% of individuals with HOD

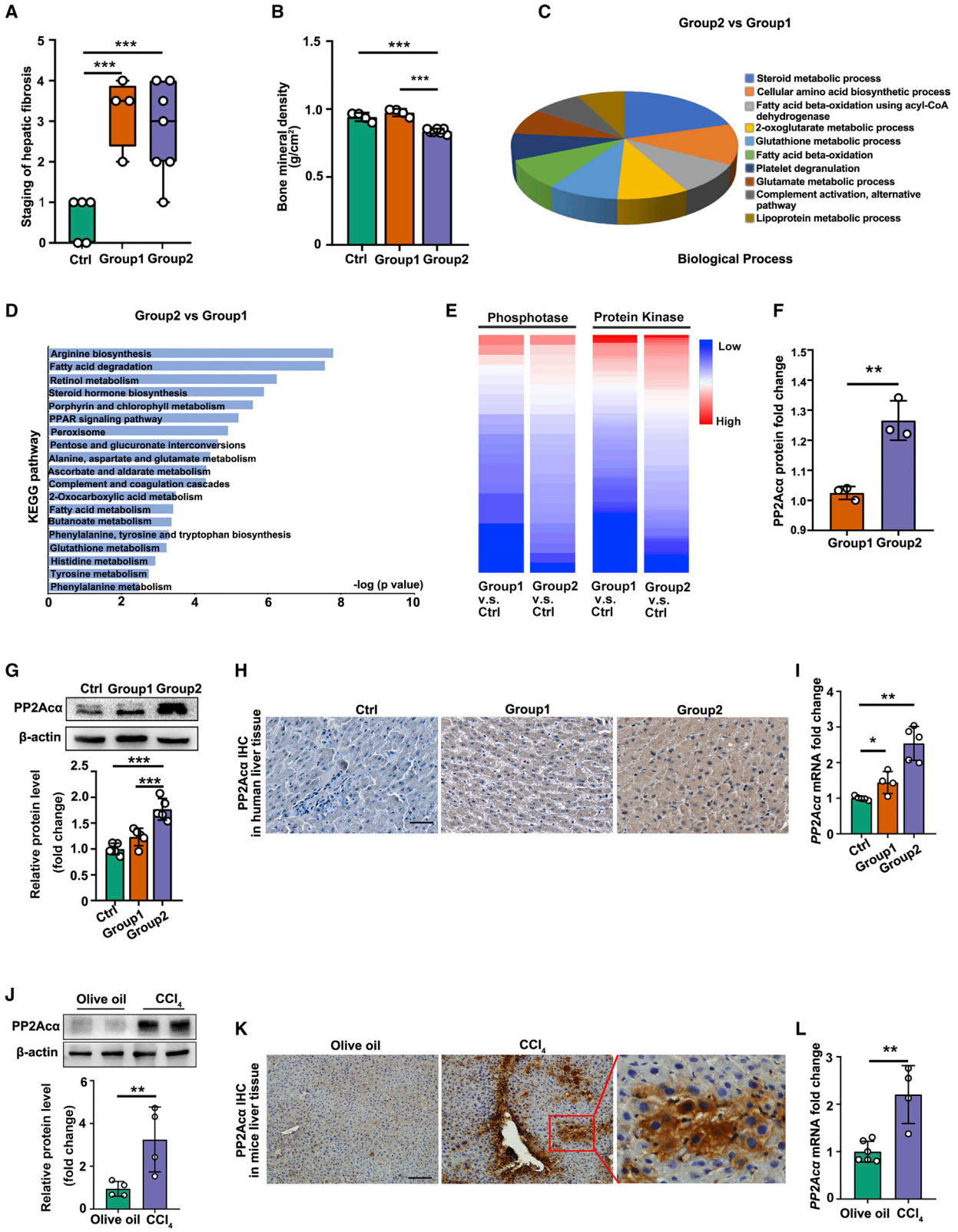

(legend on next page)

suffer from osteopenia or osteoporosis (Nussler et al., 2014). Such individuals often have symptoms of pain, bone fragility, limited mobility, and bone fractures, suggesting a disruption of proper homeostasis between the liver and bone (Barbu et al., 2017). As to the underlying mechanisms that cause HOD, chronic liver injury triggers changes in both the metabolism and the secretory function of the organ, such as inflammatory factors and hepatokines, leading to subsequent loss in bone mass. For example, individuals with liver injury caused by chronic cholestasis, alcoholic or non-alcoholic liver injury, and viral hepatitis have lower serum vitamin D (VitD) and IGF1 (Barbu et al., 2017; Uretmen et al., 2005) and higher serum bilirubin, IL-6, and IL-17, resulting in an increase in bone resorption and aggravated progression of HOD (Guarino et al., 2016; Handzlik-Orlik et al., 2016; Schmidt et al., 2019).

The current clinical treatment of HOD is limited to supplementation with VitD and Ca^{2+} or treatment with bisphosphonates (Barbu et al., 2017; López-Larramona et al., 2011). But these treatments are not based on results from large multicenter randomized controlled trials (RCTs), reflecting a clearly unmet need for the treatment of HOD. Thus, understanding the molecular mechanisms regulating the defects along this liver-bone axis is key for the development of a more effective treatment for this disease (Ehnert et al., 2019).

As a crucial member of the protein phosphatase family, PP2A regulates 90% of the dephosphorylation events of eukaryotic proteins (Eichhorn et al., 2009). The PP2A catalytic subunit, PP2Acα, plays an important role in the Ca^{2+} equilibrium of myocardial cells (Lei et al., 2015) and insulin resistance of skeletal muscles (Obanda et al., 2016). In addition, PP2A is also important for cytokine secretion (Baskaran and Velmurugan, 2018). For example, inhibition of the expression of PP2A in nerve cells significantly reduces the secretion of brain-derived neurotrophic factor (BDNF), which affects the normal physiological functions of these cells (Atasoy et al., 2017). Moreover, PP2Acα plays an important role in liver injury and liver regeneration. Notably, PP2Acα alleviates carbon tetrachloride (CCl_4)-induced acute liver injury through regulation of the TGFβ-Smad pathway (Lu et al., 2015).

In previous studies, we found that PP2Acα is involved in liver regeneration through an AKT-GSK3β-Cyclin D1 pathway (Lai et al., 2016). Meanwhile, knockout of PP2Acα in the liver significantly increases insulin sensitivity and alleviates peripheral insulin resistance (Xian et al., 2015). However, it is still unknown whether the regulation of PP2Acα expression in the liver affects bone metabolism. In this study, we use a proteomics-based approach to analyze changes in protein expression in the livers of individuals with HOD. We find a significant increase in PP2Acα protein expression and significant changes in protein phosphorylation. In addition, serum proteomic analysis reveals higher levels of LCAT expression in PP2Acα conditional knockout (cKO) mice after CCl_4-induced injury. Therefore, we propose that liver PP2Acα expression may affect bone metabolism through LCAT. These results help clarify the pathogenesis of HOD, while elucidating the mechanism of a new metabolic signaling axis between the liver and the bone, which may reveal a new therapeutic target for the treatment of HOD.

RESULTS

The upregulation of liver PP2Acα correlates with HOD severity

To identify critical molecules in the liver that may trigger bone loss during HOD, we collected liver tissues from age-matched individuals with hepatic hemangioma (as a control group) and liver cirrhosis with either normal bone mineral density (BMD) (as Group1) or low BMD (as Group2) (Figures 1A and 1B) from the Liver and Gallbladder Research Center of Drum Tower Hospital (Table S1). Individuals in Group2 were clinically diagnosed with HOD. We used high-performance liquid chromatography and mass spectrometry (HPLC-MS) for proteomic analysis of these clinical samples. The subsequent Gene Ontology (GO) analysis showed significant upregulation of steroid metabolism, cellular amino acid biosynthesis, and fatty acid (FA) β-oxidation in Group2 compared to Group1 (Figures 1C, S1A, and S1B). According to GO analysis and KEGG pathway assignment, we found that expression of proteins involved in energy metabolism, such as proteins related to FA degradation and steroid hormone

Figure 1. The upregulation of liver PP2Acα correlates with HOD severity

(A and B) The stages of hepatic fibrosis (A) and bone mineral density (BMD) (B) of individuals from control group (n = 5), Group1 (n = 4), and Group2 (n = 7). The liver tissues were collected from age-matched individuals with hepatic hemangioma (as control group) and liver cirrhosis with normal BMD (as Group1) and individuals with liver cirrhosis and low BMD (as Group2 or HOD group).

(C and D) Analysis of biological process (C) and KEGG pathway (D) from upregulation of liver proteins in Group2 compared to Group1 (1 technical replicate of 3 biological replicates per group).

(E) Comparative analysis of phosphatase and protein kinase between Group2 and Group1 (1 technical replicate of 3 biological replicates per group).

(F) Fold changes in PP2Acα expression in Group2 compared with Group1 (n = 3 paired biological replicates).

(G) Representative western blots (n = 5 in total) of PP2Acα expression in liver tissues of individuals (top) and its quantification (bottom).

(H) Representative IHC of PP2Acα expression in liver tissues of the groups indicated (control, n = 5; Group1, n = 4; Group2, n = 5; 20 areas per individual were analyzed).

(I) qRT-PCR of relative *PP2Acα* mRNA levels of the groups indicated, with the level in the control group arbitrarily set to 1 (control, n = 5; Group1, n = 4; Group2, n = 5).

(J) Representative western blots (n = 4 in total) of PP2Acα expression in a mouse model of liver injury after low doses of CCl_4 injection for 6 weeks (top) and its quantification (bottom) (olive oil, 2 technical replicates of 2 biological replicates; CCl_4, 2 technical replicates of 2 biological replicates).

(K) Representative IHC of PP2Acα expression in liver tissues of a mouse model of liver injury after low doses of CCl_4 injection for 6 weeks (scale bar, 200 μm) (olive oil, n = 6; CCl_4, n = 4; 7 areas per mouse were analyzed).

(L) qRT-PCR of relative PP2Acα mRNA levels of the groups indicated, with the level in the olive oil group arbitrarily set to 1 (olive oil, n = 6; CCl_4, n = 4).

*p < 0.05, **p < 0.01, ***p < 0.001; NS, no significant difference. Rank-sum test (A), two-tailed Student's unpaired t test (F, J, and L), or one-way ANOVA followed by Tukey's multiple comparisons test (B, G, and I). Data are represented as mean ± SEM.

See also Figure S1 and Table S1.

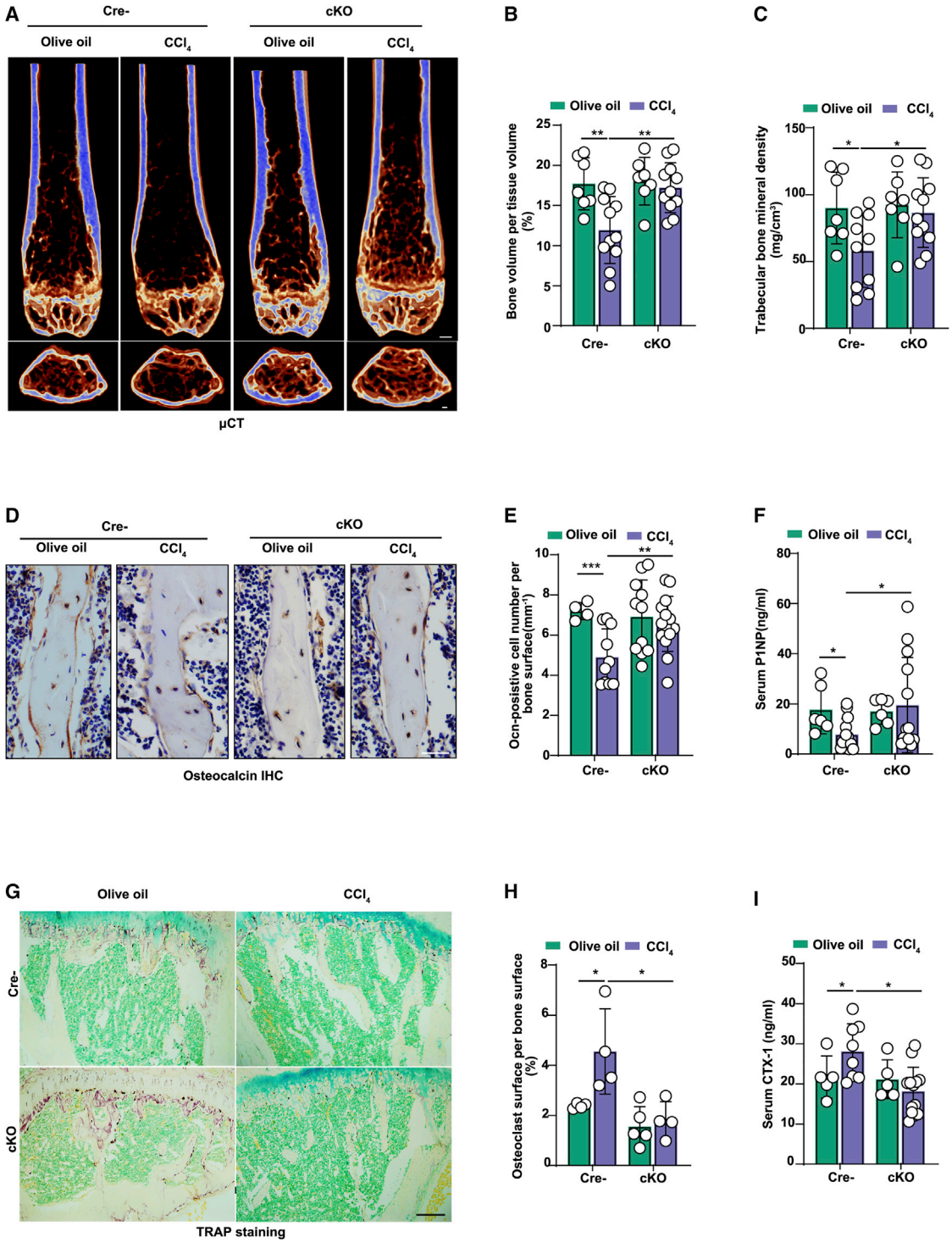

Figure 2. Liver-specific deficiency of *PP2Acα* ameliorates bone loss in HOD mice

(A–C) Representative 3D structure images of the μCT analysis of trabeculae of femora (scale bar, 1 mm [coronal section]; 100 μm [transversal section]) (A), value of the bone volume per tissue volume (%) (B), and trabecular BMD (C) (olive oil + Cre$^-$, n = 7; olive oil + cKO, n = 7; CCl_4 + Cre$^-$, n = 10; CCl_4 + cKO, n = 11).

(D and E) Representative images of IHC staining (D) for detecting the osteocalcin (Ocn) expression, which reflects the osteoblast activity (scale bar, 50 μm). Analysis of Ocn-positive cell number per bone surface (E) (olive oil + Cre$^-$, n = 4; olive oil + cKO, n = 11; CCl_4 + Cre$^-$, n = 10; CCl_4 + cKO, n = 14; 7 areas per mouse were analyzed).

(F) Detection of serum P1NP, which reflects the bone formation detected by ELISA (n = 6–12).

(legend continued on next page)

biosynthesis, was notably upregulated (Figure 1D). The data suggest that individuals with HOD exhibit an elevation in hepatic cellular energy metabolism compared to individuals with cirrhosis without bone loss (Shergill et al., 2018).

As protein phosphorylation is important for the proper regulation of cellular metabolism (Humphrey et al., 2015), we performed proteomic analysis and found significant changes in the expression of kinases and phosphatases between Group2 and Group1 (Figure 1E). Among them, the α catalytic submit of PP2A increased about 30% in the samples from Group2 compared to Group1 (Figure 1F). We confirmed these finding by western blotting, immunohistochemistry (IHC), and RT-PCR analyses of the clinical samples (Figures 1G–1I).

To further verify these results, we generated a mouse model of HOD by injuring their livers with CCl_4 treatment (Nussler et al., 2014). We observed liver injury and fibrotic formation after CCl_4 exposure for 1 week (Figures S1C–S1E), while trabecular BMD downregulation was detected at 3 weeks (Figures S1C and S1F). Consistent with the human clinical data, PP2Acα in the liver of the HOD mice also increased significantly at 6 weeks after CCl_4 treatment (Figures 1J–1L). Besides changes in PP2Acα expression, we also detected other changes in phosphatase and protein kinase gene expression between Group1 and Group2 by RT-PCR (Figure S1G).

Hepatocyte-specific *PP2Acα* deficiency ameliorates osteoporosis in HOD mice

As high levels of PP2Acα were found in the liver of individuals with HOD and in the mouse model, we generated hepatocyte-specific *PP2Acα* cKO mice to explore the effects of liver PP2A on bone metabolism (Lai et al., 2016; Xian et al., 2015). Compared with the Cre^- control mice, hepatocyte-specific *PP2Acα*-deficient mice were highly resistant to CCl_4-induced bone loss by μCT analysis (Figure 2A). Further analysis revealed that the bone volume per tissue volume (%, BV/TV) and BMD were both elevated by about 30% in *PP2Acα* cKO mice compared with the Cre^- control mice (Figures 2B and 2C). Moreover, The *PP2Acα* cKO mice showed an increase in trabecular number (Tb.N., 27% increase), trabecular thickness (Tb.Th., 36% increase), and cortical thickness (Co.Th., 15% increase) compared to the Cre^- control group, along with significant decreases in trabecular separation (Tb.Sp., 63% decrease) (Figures S2A–S2E) (Parfitt et al., 1987).

Considering the imbalance between bone formation and bone resorption in HOD, we further examined the biomarkers of osteoblasts and osteoclasts. *PP2Acα* cKO mice maintained the normal bone formation compared to the Cre^- control mice, as analyzed by the histomorphometric measurements of osteoblast numbers, P1NP detection, and calcein double labeling (Figures 2D–2F, S2F, and S2G). Consistently, *PP2Acα* cKO mice were resistant to bone resorption (Figures 2G–2I), as analyzed by TRAP staining and CTX-1 detection.

We then transfected the mouse hepatocyte cell line AML12 with LV-*shPP2Acα* (Figure S2H) and collected conditioned medium (CM) to treat MC3T3-E1 cells (pre-osteoblast cell line) and RAW264.7 cells (pre-osteoclast cell line). We found *Runx2*, *Sp7*, and *Alp* expression was significantly upregulated in MC3T3-E1 cells in a dose-dependent manner (Figure S2I), while expression of the osteoclast markers *Trap*, *Ctsk*, and *Oscar* was downregulated after RAW264.7 cells were treated with LV-*shPP2Acα*-CM (Figure S2J).

Hepatocyte-specific *PP2Acα* deficiency leads to elevation of LCAT and alleviation of HOD

Because hepatocyte-specific *PP2Acα* deficiency ameliorates the bone loss phenotype induced by CCl_4, we hypothesized that molecule(s) produced in the liver downstream of PP2Acα activity may inhibit the bone loss phenotype. Therefore, we collected serum from both *PP2Acα* cKO mice and Cre^- control CCl_4-induced liver injury mice for HPLC-MS detection. Proteomic analysis identified 122 differentially expressed proteins in CCl_4-induced liver injury mice, several of which are involved in cell proliferation, cholesterol transport, cholesterol efflux, and lipid metabolism (Figures 3A and 3B). Consistent with these findings, cellular component and molecular function analysis also showed that lipoproteins contribute to a large proportion of the protection from bone loss observed in the *PP2Acα* cKO mice (Figures S3A and S3B), suggesting that regulation of lipid metabolism may contribute to the control of bone mass mediated by hepatic PP2A.

To screen the candidate(s) that could regulate both the liver and bone functions, we used a volcano plot visualization technique to observe differentially expressed proteins in the serum of *PP2Acα* cKO mice and compared with that of Cre^- control mice (Figure 3C). Based on the differential expression pattern, we conducted a comprehensive screening according to following considerations: (1) whether the candidate was a liver-specific protein secreted during liver injury, (2) whether this protein is involved in lipid metabolism and bone homeostasis, and (3) whether this protein has a potential translational value. Finally, four genes (*Lcat*, *Lifr*, *Serpinf1*, and *Elastase*) were selected for further experimentation.

We found that the expression of *Lifr*, *Serpinf1*, and *Elastase* was not increased in primary hepatocytes isolated from *PP2Acα* cKO mice that had been injured with CCl_4 (Figures S3C–S3E). Interestingly, the expression of LCAT, a hepatokine known to regulate the metabolism of cholesterol through promotion of reverse transport (van der Velde, 2010), was increased 1.4-fold in *PP2Acα* cKO mice compared to Cre^- mice with CCl_4 treatment by mass spectrometry analysis (Figure 3C). Consistent with the results of the proteomic analysis, the serum levels of LCAT increased 30% in *PP2Acα* cKO mice compared with those in Cre^- control mice (Figure 3D).

(G and H) Representative images of TRAP staining (G) (scale bar, 200 μm) and analysis of osteoclast surface per bone surface (H) for detecting the matured osteoclasts (olive oil + Cre^-, n = 4; olive oil + cKO, n = 5; CCl_4 + Cre^-, n = 4; CCl_4 + cKO, n = 4; 7 areas per mouse were analyzed).

(I) Detection of serum CTX-1, which reflects the bone resorption detected by ELISA (n = 5–12).

*p < 0.05, **p < 0.01, ***p < 0.001; NS, no significant difference. Two-way ANOVA followed by Tukey's multiple comparisons test (B, C, E, F, H, and I). Data are represented as mean ± SEM.

See also Figure S2.

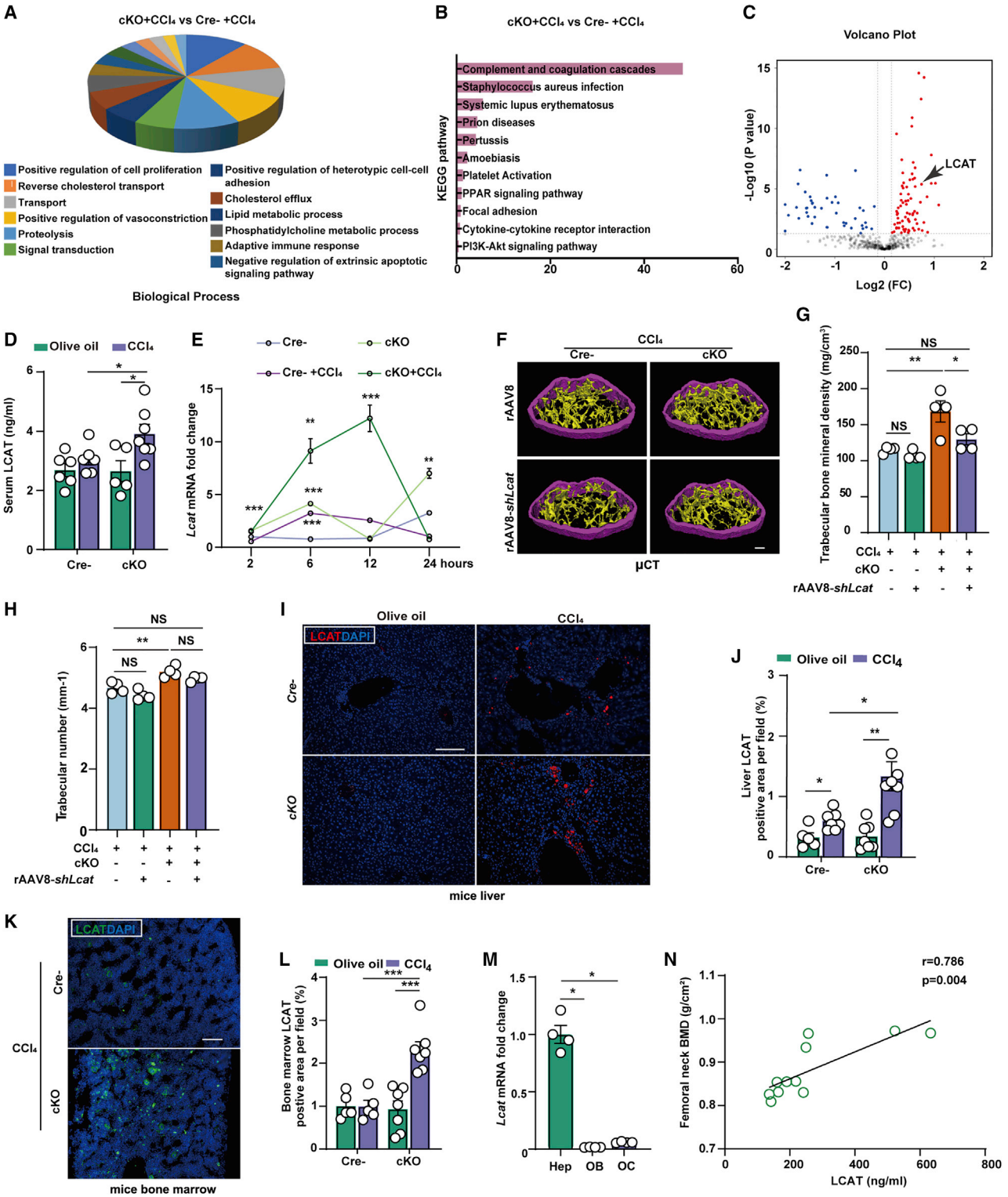

Figure 3. Liver-derived LCAT induced by *PP2Acα* deficiency ameliorates HOD

(A and B) Ratio of upregulated serum proteins in *PP2Acα* cKO versus Cre$^-$ control mice under CCl_4 induction using biological process (A) and KEGG pathway (B) analyses (2 technical replicate of 3 paired biological replicates).

(C) Ratio of altered serum proteins in *PP2Acα* cKO versus Cre$^-$ control mice under CCl_4 induction using volcano plot analysis.

(D) Serum LCAT levels in *PP2Acα* cKO and Cre$^-$ control mice with or without CCl_4 induction detected by ELISA (1 technical replicate of n = 5–7 biological replicates per group).

(legend continued on next page)

It has been reported that free cholesterol inhibits BMP2 from blocking the expression of *Runx2*, *Alp*, and *Col1a1* in osteoblasts and inhibits osteoblast differentiation (Yin et al., 2019). Thus, we postulated that LCAT may be the hepatokine responsible for the bone loss protection observed in hepatocyte-specific *PP2Acα*-deficient mice. We isolated mouse primary hepatocyte derived from chronic injured liver induced by CCl_4. We found that *Lcat* mRNA levels are slightly higher in hepatocytes of *PP2Acα* cKO mice compared to Cre^- mice under physiological condition (i.e., without liver injury). Treatment with CCl_4 further induced a 10-fold increase in *Lcat* expression in primary hepatocytes of *PP2Acα* cKO mice compared to uninjured cKO mice (Figure 3E). To explore whether PP2Acα regulates LCAT expression, we infected AML12 cells with different doses of LV-*shPP2Acα* and found that *Lcat* expression was significantly upregulated in a dose-dependent manner (Figure S3F).

To further determine whether LCAT is required for preventing bone loss in *PP2Acα* cKO mice, we injected recombination adeno-associated virus 8 short hairpin *Lcat* (rAAV8-*shLcat*) into the tail vein (2^{11} titer, single injection) of *PP2Acα* cKO mice 2 weeks before CCl_4 induction (CCl_4 was mixed with olive oil, 1 mL/kg body weight) (Figure S3G). By μCT analysis we found that the inhibition of LCAT in *PP2Acα* cKO mice had the same degree of bone loss observed in control mice (Figures 3F, 3G, and S3H). Consequently, we found no differences in BV/TV, Tb.Th., Tb.Sp., and Tb.N. between the knockout treated with rAAV8-*shLcat* and rAAV8 control mice (Figures 3H and S3I–S3K), indicating that upregulation of LCAT in *PP2Acα*-deficient mice contributes to the alleviation of the bone loss in our HOD model.

To investigate the transportation of LCAT from the liver to the bone marrow during the development of HOD, we analyzed the distribution of LCAT in the liver and bone using immunofluorescence. As expected, we found the increased LCAT expression in liver tissue and a greater distribution of LCAT in the bone marrow in *PP2Acα* cKO mice compared to the Cre^- control mice (Figures 3I–3L). We then confirmed that the increased LCAT in the bone marrow was specifically produced and transported from the liver. RT-PCR analysis revealed much lower *Lcat* expression in osteoblasts and osteoclasts compared to the hepatocytes (Figure 3M). Moreover, the expression of *Lcat* mRNA was significantly greater in the liver compared to bone and other tissues of wild-type (WT) mice (Figure S3L), suggesting that LCAT might be acting as a hepatokine to impact bone mass regulation. These data demonstrated that hepatocyte-specific *PP2Acα* deficiency results in the upregulation of LCAT expression in hepatocytes.

We investigated the correlation between serum LCAT levels and femoral neck BMD in individuals with HOD and observed higher serum LCAT levels, which are correlated with greater femoral neck BMD in individuals with HOD (Figure 3N) ($r = 0.786$, $p = 0.004$), suggesting that levels of LCAT are positively correlated with BMD in individuals with HOD.

PP2Acα regulates LCAT expression through dephosphorylation of transcription factor USF1

To further explore the molecular mechanisms underlying LCAT upregulation in *PP2Acα* deficiency, we performed bioinformatics analysis of transcription factors that may bind to the *Lcat* promoter with information about proteomic analysis of liver protein phosphorylation. Through this analysis, we identified nine candidate transcription factors for further study (Figure 4A).

Based on the analysis of ratio of upregulation to the binding score (Table S2), we selected USF1 as a candidate to further determine its transcriptional activity on *Lcat* regulation in hepatocytes. We transfected AMF12 cells with USF1 small-interfering RNA (*siUsf1*) or control scrambled siRNA. Inhibition of USF1 significantly increased mRNA levels of *Lcat* (Figure 4B). As PP2Acα is a critical phosphatase in the negative regulation of protein phosphorylation, we hypothesized that PP2Acα directly dephosphorylated USF1 to affect LCAT expression. Using a co-immunoprecipitation (coIP) assay, we found that PP2Acα directly interacts with USF1 (Figure 4C), and *PP2Acα* deficiency promotes the elevation of phospho-USF1 levels as detected by an anti-p(Ser/Thr)-Phe antibody (Figure 4D). Further, through a phosphorylation assay, we found that deletion of *PP2Acα* significantly increased the level of phosphorylated USF1 (Thr153) without affecting the total amount of USF1 protein (Figure 4E), suggesting that PP2Acα modifies USF1 protein dephosphorylation. The above results indicate that the phosphorylation of USF1 is key for its transcriptional activity, as previously reported (Galibert et al., 2001). Consistent with these findings, we found that mutation of the Thr153 in USF1 completely abrogated the effect

(E) qRT-PCR of relative *Lcat* mRNA levels in primary hepatocytes derived from *PP2Acα* cKO and Cre^- control mice treated with or without 1 μM CCl_4 for different times as indicated (1 technical replicate of n = 4 biological replicates per group).
(F–H) μCT representative images (F) (scale bar, 400 μm) and quantification of bone mineral density (G) and the trabecular numbers (H) of WT mice treated with CCl_4 followed by CCl_4 induction 2 weeks after *shLcat* administration (1 technical replicate of n = 4 biological replicates per group).
(I and J) Representative images of immunofluorescence (IF) staining of liver LCAT (I) (scale bar, 100 μm) and quantification of liver LCAT-positive area per selective field (J) in *PP2Acα* cKO and Cre^- control mice with or without CCl_4 induction (1 technical replicate of n = 5–7 biological replicates per group, 7 areas per mouse were analyzed).
(K and L) Representative images of IF staining of LCAT in bone marrow in *PP2Acα* cKO and Cre^- control mice with CCl_4 induction (scale bar, 100 μm) (K) and quantification of LCAT-positive area (L) per selective field in the bone marrow of *PP2Acα* cKO and Cre^- control mice with or without CCl_4 induction (1 technical replicate of n = 5–7 biological replicates per group, 7 areas per mouse were analyzed).
(M) qRT-PCR of relative *Lcat* mRNA levels of the groups in primary hepatocytes compared with that in primary osteoblasts and primary osteoclasts (1 technical replicate of n = 4 biological replicates per group).
(N) Correlation analysis between the level of serum LCAT and the femoral neck BMD in individuals with cirrhosis (1 technical replicate of n = 11 biological replicates per group).
*p < 0.05, **p < 0.01, ***p < 0.001; NS, no significant difference. Two-way ANOVA followed by Tukey's multiple comparisons test (D, E, G, H, J, and L), one-way ANOVA followed by Tukey's test (M), and Spearman's correlative analysis (N). Data are represented as mean ± SEM.
See also Figure S3.

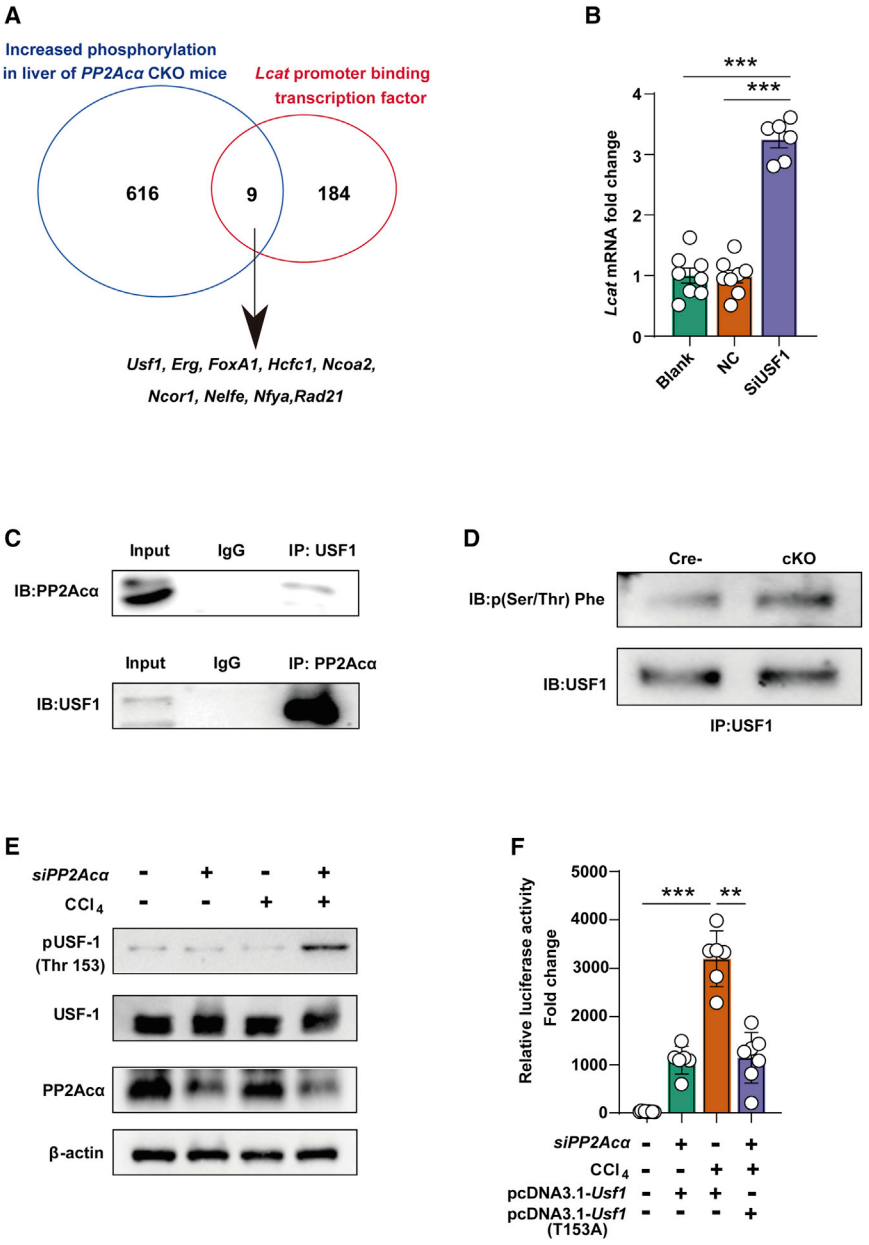

Figure 4. PP2Acα regulates LCAT expression through dephosphorylation of the transcription factor USF1

(A) Screening map of the increase of phosphorylated proteins in the liver of *PP2Acα* cKO mice and the transcription factors bound to *Lcat* promoter.

(B) qRT-PCR of relative *Lcat* mRNA levels of the groups in AML12 cells transfected with *siUsf1* (1 technical replicate of n = 6–8 biological replicates per group).

(C) Representative immunoblots (n = 3 in total) of the coIP assay between PP2Acα and USF1.

(D) Representative immunoblots (n = 3 in total) of the increased phosphorylation of USF1 in the liver of *PP2Acα* cKO mice.

(E) Representative immunoblots (n = 4 in total) of the increased phosphorylation of USF1 at Thr153 site in AML12 cells transfected with *siPP2Acα* followed by CCl_4 treatment.

(F) LCAT luciferase activity of the groups indicated, with the level in the blank group arbitrarily set to 1 (1 technical replicate of n = 6–7 biological replicates per group).

**p < 0.01, ***p < 0.001; NS, no significant difference. One-way ANOVA followed by Tukey's multiple comparisons test (B and F). Data are represented as mean ± SEM.

See also Table S2.

of *siPP2Acα* on *Lcat* transcriptional activation by luciferase assay (Figure 4F).

Liver-derived LCAT improves HOD through regulation of bone homeostasis

Bone homeostasis is maintained by a balance between bone resorption mediated by osteoclasts and bone formation mediated by osteoblasts (Eastell et al., 2016). To explore whether liver-produced LCAT regulates bone homeostasis, we transfected *siLcat* or *Lcat* plasmids in AML12 cells and collected CM to treat MC3T3-E1 cells or RAW264.7 cells (Figure 5A). We detected increased Collagen1 levels and ALP staining in MC3T3-E1 cells after treatment with CM collected from cells transfected with the *Lcat* plasmid (Figures 5B, 5C, and S4A). LCAT significantly augmented osteoblast differentiation by upregulating *Runx2*, *Sp7*, and *Alp* expression (Figure 5E) (Karner et al., 2017; Wei et al., 2015). In contrast, LCAT inhibited osteoclast differentiation by reducing TRAP, *Ctsk*, *Oscar*, and *Mmp9* expression (Amarasekara et al., 2018) (Figures 5B and 5F). In addition, LCAT knockdown significantly stimulated the osteoclast differentiation (Figures 5D and S4B).

To determine whether LCAT sufficiently regulates osteoclast or osteoblast function, we purchased active recombinant LCAT (rLCAT) protein and treated primary osteoblasts and osteoclasts with rLCAT (Figure S4C). As expected, rLCAT enhanced osteoblast differentiation by increasing *Runx2*, *Sp7*, *Col1a2*, and *Ocn* expression, as well as ALP staining (Figures 5G, 5H, and S4D). We further confirmed these data by western blot analysis (Figure 5I). We found that PCNA expression was upregulated after rLCAT treatment for 48 h (Figure 5I), indicating that LCAT may regulate osteoblast proliferation. In contrast, recombinant LCAT reduced the expression of *Trap*, *Ctsk*, and *Oscar* in osteoclasts, inhibited osteoclast formation in a dose-dependent manner, and decreased the TRAP staining-positive area (Figures 5J and 5K). Consistent with these findings, western blot analysis revealed a significant decrease in CTSK and TRAP expression after rLCAT treatment for 24 and 48 h (Figure 5L).

We next investigated whether LCAT regulates bone homeostasis *in vivo*. For a gain-of-function approach, we administered rAAV8-*Lcat* into HOD mice for 2 months (Figure S4E). Tail vein

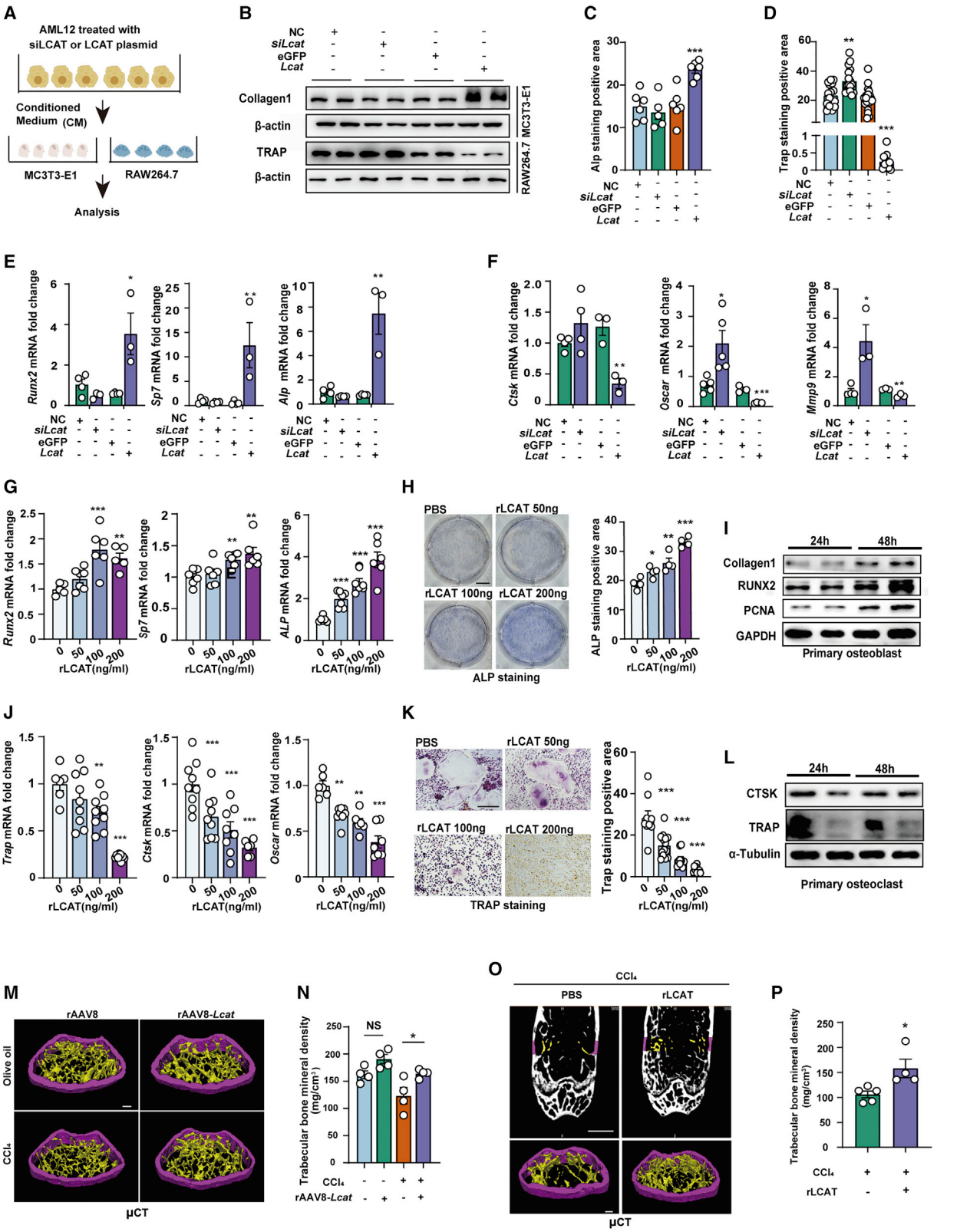

(legend on next page)

rAAV8-*Lcat* injection significantly upregulated bone mass in HOD mice by μCT analysis of the proximal tibiae (Figures 5M, 5N, and S4F). Consequently, BMD increased by more than 20% compared to the control group (Figure 5N) and the corresponding BV/TV increased by more than 30% compared to the control group as indicated (Figure S4G). The results of Tb.Th., Tb.N., and Tb.Sp. analyses showed only a slight increase with no significant changes compared with those in the control group as indicated (Figures S4H–S4J). Consistent with the results of rAAV8-*Lcat* injection, we used rLCAT to examine the direct effect of LCAT on relieving the development of HOD. Two months after rLCAT tail vein injection (every 2 days per injection, total 24 injections), the bone loss in mice with HOD was rescued in the treatment group (Figures 5O, 5P, and S4K–S4O).

LCAT maintains proper intracellular cholesterol levels to alleviate defects in osteoblasts and osteoclasts

We next investigated the molecular mechanism by which LCAT regulates bone homeostasis. LCAT, as a lecithin:cholesterol acyltransferase, has been considered the "engine" to create a gradient necessary for transferring unesterified cholesterol from peripheral tissues back to the liver during reversing cholesterol transport (Saeedi et al., 2015; van der Velde, 2010). Using Filipin III (Maxfield and Wüstner, 2012) and Nile Red staining (Amini-Bavil-Olyaee et al., 2013), we observed that intracellular cholesterol is located in the cytoplasm of primary osteoclasts isolated from mice (Figures 6A and S5A). Addition of rLCAT to the culture medium significantly decreases the intracellular cholesterol compared to the PBS control, similar to the positive control in which the cholesterol-binding hydroxypropyl cyclodextrin (HPCD) was added to the culture medium (Figures 6A and S5A) (Wei et al., 2016). More importantly, we found that adding rLCAT inhibited osteoclastogenesis. Following cholesterol treatment could reverse the inhibition effect of rLCAT on osteoclasts. (Figures 6B–6D). In osteoclasts, cholesterol acts as an ERRα ligand and promotes the expression of ERRα target genes to enhance osteoclast differentiation (Wei et al., 2010, 2016). As expected, rLCAT inhibited the expression of ERRα targeted genes that stimulate mitochondrial biogenesis and osteoclast activity, such as *Idh3a*, *Vlcad*, and *Aco2*, which was abolished by adding back cholesterol (Figures 6E–6G). These data suggest that LCAT inhibits osteoclastogenesis in a cholesterol-dependent manner.

Consistent with the above observations, we found that treatment of osteoblasts with both rLCAT and HPCD decreased intracellular cholesterol (Figures 6H and S5B). Addition of cholesterol inhibited osteoblast differentiation by decreasing mRNA levels of osteoblast marker genes compared to the PBS control, whereas addition of rLCAT to the cholesterol-treated cells was able to rescue the osteoblast differentiation (Figures 6I–6N), indicating that cholesterol was responsible for the LCAT-induced bone formation.

Next, we collected serum samples derived from normal individuals and those with HOD and added different concentrations of LCAT antibody. We then added the serum treated with LCAT antibody to cultures of primary osteoblasts or osteoclasts and found that the expression of osteoblast markers (*Runx2*, *Alp*, and *Col1a2*) was downregulated with increasing concentrations of LCAT antibody (Figures S5C–S5E). In contrast, LCAT antibody treatment restored the expression of *Trap*, *Ctsk*, and *Oscar* among the osteoclast cultures in a dose-dependent manner (Figures S5F–S5H).

Figure 5. Liver-derived LCAT improves HOD by rebalancing bone homeostasis

(A) A schematic diagram demonstrating culture of MC3T3-E1 and RAW 264.7 cells treated with conditioned medium (CM) collected from AML12 cells.

(B) Representative western blots of Collagen 1 in MC3T3-E1 cells and representative western blots of TRAP in RAW 264.7 cells treated with CM collected from AML12 cells transfected with *siLcat* or *Lcat* plasmid (pcDNA3.1-*Lcat*) for 12 h. Scrambled siRNA was used as a control of *siLcat* and pcDNA3.1-e*GFP* served as a control of *Lcat* plasmid transfection (3 technical replicates of 2 biological replicates).

(C and D) Quantification of ALP staining in primary osteoblasts (C) (1 technical replicate of n = 5–6 biological replicates per group) and TRAP staining in primary osteoclasts (D) (1 technical replicate of n = 11–21 biological replicates per group) treated with CM collected from AML12 cells transfected with *siLcat* or *Lcat* plasmid for 48 h.

(E) qRT-PCR of relative osteoblast marker (*Runx2*, *Sp7*, and *Alp*) mRNA levels of the groups indicated in MC3T3-E1 cells, with the level in the NC group arbitrarily set to 1 (1 technical replicate of n = 3–4 biological replicates per group).

(F) qRT-PCR of relative osteoclast marker (*Ctsk*, *Oscar*, and *Mmp9*) mRNA levels of the groups indicated in RAW 264.7 cells, with the level in the NC group arbitrarily set to 1 (1 technical replicate of n = 3–4 biological replicates per group).

(G) qRT-PCR of relative osteoblast marker (*Runx2*, *Sp7*, and *Alp*) mRNA levels in primary osteoblasts after cells were treated with 50, 100, and 200 ng/mL rLCAT for 24 h, with the level in the blank group (0 ng/mL rLCAT treatment) arbitrarily set to 1 (1 technical replicate of n = 5–8 biological replicates per group).

(H) ALP staining for the primary osteoblasts treated with 50, 100, and 200 ng/mL rLCAT for 7 days (scale bar, 1 cm) (1 technical replicate of n = 4 biological replicates per group, 7 areas per biological replicate were analyzed).

(I) Representative western blots (n = 3 in total) of the expression of Collagen1, RUNX2, and PCNA proteins in primary osteoblasts treated with rLCAT for 24 and 48 h.

(J) qRT-PCR of relative osteoclast marker (*Trap*, *Ctsk*, and *Oscar*) mRNA levels in primary osteoclasts after cells were treated with 50, 100, and 200 ng/mL rLCAT for 24 h, with the level in the blank group (0 ng/mL rLCAT treatment) arbitrarily set to 1 (1 technical replicate of n = 6–9 biological replicates per group).

(K) Representative TRAP staining of the primary osteoclasts treated with 50, 100, and 200 ng/mL rLCAT for 14 days (scale bar, 500 μm) (1 technical replicate of n = 9–11 biological replicates per group, 7 areas per biological replicate were analyzed).

(L) Representative western blots (n = 3 in total) of the protein levels of CTSK and TRAP in primary osteoclasts treated with rLCAT for 24 and 48 h.

(M and N) μCT representative images (M) and BMD quantifications (N) of WT mice injected with or without rAAV8-*Lcat* 2 weeks later, followed by CCl_4 induction for 6 weeks. Olive oil was used as a control of CCl_4 (1 technical replicate of n = 4 biological replicates per group).

(O and P) μCT representative images (O) (scale bar, 1 mm [coronal section]; 400 μm [transversal section]) and quantification of BMD (P) of WT mice treated with CCl_4 followed by rLCAT administration once a week for 6 weeks (1 technical replicate of n = 4–5 biological replicates per group).

*p < 0.05, **p < 0.01, ***p < 0.001; NS, no significant difference. One-way ANOVA followed by Tukey's test (C–H, J, and K), two-way ANOVA followed by Tukey's post-test for multiple comparisons (N), and two-tailed Student's unpaired t test analysis (P). Data are represented as mean ± SEM.

See also Figure S4.

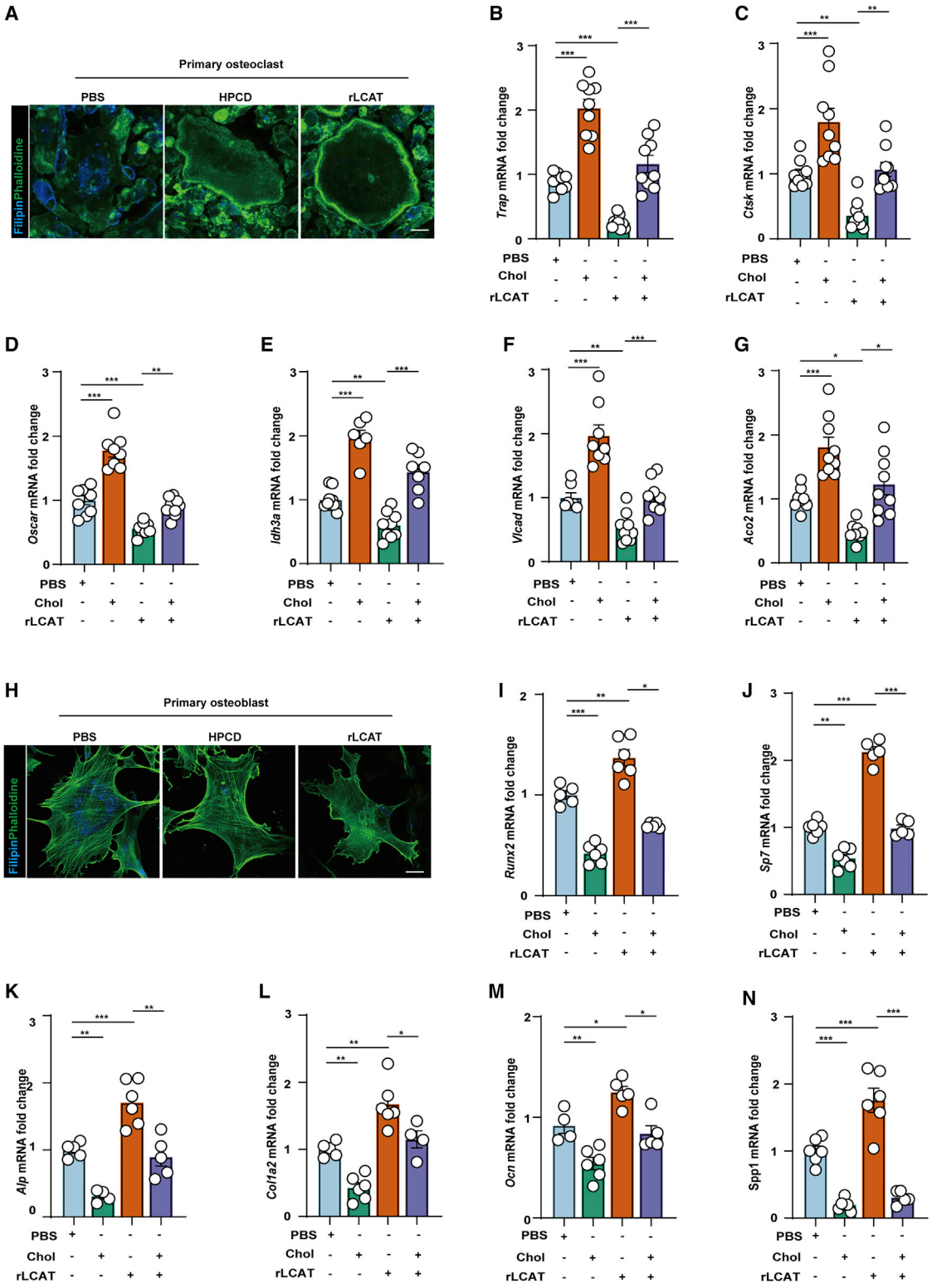

Figure 6. LCAT maintains proper intracellular cholesterol levels to alleviate the metabolic disorders of bone tissues

(A) Filipin III staining of intracellular cholesterol in primary osteoclasts treated with rLCAT for 24 h (scale bar, 50 μm) (1 technical replicate of 3 biological replicates per group).

(B–G) qRT-PCR of relative osteoclast marker gene (*Trap*, *Ctsk*, and *Oscar*) and estrogen-related receptor alpha (ERRα) targeted gene (*Idh3a*, *Vlcad*, and *Aco2*) mRNA levels of the groups indicated, with the level in the PBS group arbitrarily set to 1 (1 technical replicate of n = 6–9 biological replicates per group).

(legend continued on next page)

We also used an LCAT inhibitor (DTNB) to explore the function of LCAT and found that treatment with DTNB aggravated the HOD phenotype in WT mice and eliminated the protective effect of *PP2Acα* KO in the mice with CCl_4-induced liver injury. Treatment with DTNB also aggravated the fibrosis phenotype and upregulated levels of serum ALT and AST in cKO mice (Figures S6A–S6E), and bone mass markers (i.e., BMD, BV/TV, and Tb.Th.) deteriorated in *PP2Acα* cKO mice after DTNB treatment (Figures S6F–S6I).

LCAT benefits the recovery of liver injury in HOD through promotion of reverse cholesterol transportation

As LCAT-mediated reverse cholesterol transport is responsible for transferring cholesterol from peripheral tissues to the liver, where it utilized by hepatocytes for energy metabolism, we hypothesized that the cholesterol transported from the bone tissue by LCAT may play a pivotal role in liver recovery after injury. The fur of mice often excites background noise, which is confused with the target signal; thus, we choose nude mice for further *in vivo* optical imaging study. To test the role of the reverse cholesterol transport pathway from bone to liver in this recovery process, we injected NBD-cholesterol into the bone marrow of HOD nude mice (Figure 7A) (Song et al., 2015). Two hours after NBD-cholesterol was injected into the bone marrow, we injected rLCAT or PBS into the tail vein for 6, 24, and 48 h (Figure 7A). As expected, the results of fluorescence imaging analysis showed that NBD-cholesterol in the PBS group was distributed from bone marrow to peripheral tissues and gradually concentrated in the perineum. In contrast, in the rLCAT-treated group, we detected the NBD-cholesterol mostly in the bone marrow 6 h after injection, but most of it accumulated in the liver 48 h after injection. We also performed an immuno-fluorescence assay using the frozen sections of the livers, and the fluorescence signal of NBD-cholesterol in hepatocytes was observed in the rLCAT group, but not in the PBS-injected controls, by laser scanning confocal microscopy (Figure S7A).

To further confirm if LCAT enhances the translocation of bone-derived cholesterol to the injured liver, we conducted *in vitro* co-culture experiments (Figure 7B). Primary osteoblasts or osteoclasts, which had phagocytized the NBD-cholesterol, were located at the upper cell layer while primary hepatocytes were located at the lower cell layer. We increased the LCAT level in the co-culture systems in two ways: by pre-treatment of hepatocytes with 1 μM CCl_4 to induce cellular injury or by adding rLCAT to the culture medium. We detected NBD-cholesterol fluorescence in hepatocytes by both means compared to the control PBS treatment group (Figures 7C and 7D).

To determine whether the bone-derived cholesterol could rescue the CCl_4-induced liver injury in *PP2Acα* cKO mice, we analyzed the liver function of the mice. *PP2Acα* deficiency exhibited a significantly improved liver function as marked by lower ALT and AST levels compared to CCl_4-injured Cre^- mice (Figures 7E and 7F) (Lai et al., 2016). Results of Sirius red staining also showed a slight reduction in liver fibrosis in *PP2Acα* cKO mice treated with CCl_4 compared to the control mice (Figures 7G and 7H). Furthermore, loss of function of LCAT by rAAV8-*shLcat* in *PP2Acα* cKO mice treated with CCl_4 completely blocked liver recovery (Figures 7I–7L and S7B), verifying that LCAT could alleviate the liver impairment in the mice with CCl_4-induced liver injury.

We next explored the therapeutic potential of targeting LCAT in the development of CCl_4-induced HOD mice. We overexpressed LCAT in CCl_4-induced HOD mice by injection of rAAV8-*Lcat*. Compared to that of rAAV8 injection, injection of rAAV8-*Lcat* relived the fibrosis phenotype and reduced the level of serum ALT (Figures 7M–7P and S7C). In addition, the tail vein injection of rLCAT into mice with HOD also showed a similar tendency of decreased liver fibrosis as well as decreased serum levels of ALT and AST (Figures 7Q–7T).

DISCUSSION

Up to now, little was known about the pathogenesis of HOD. In our study, we demonstrate that the hepatokine LCAT is negatively regulated by PP2Acα, and that restoring LCAT levels can effectively improve the symptoms of HOD. *In vivo* studies show that PP2Acα inhibition induced LCAT expression and that LCAT not only prevents bone loss, but also ameliorates chronic liver injury. Conversely, loss of function of LCAT markedly exacerbated these phenotypic changes of HOD. Mechanistically, we find that LCAT expression is negatively regulated by PP2Acα-mediated dephosphorylation of USF1. And we demonstrate that alteration of cholesterol levels is involved in the regulation of osteoblast and osteoclast activities. Additionally, LCAT improves liver fibrosis and liver function by promoting reverse cholesterol transport in HOD. Thus, we propose a new therapeutic strategy in which targeting of a PP2Acα-regulated pathway of LCAT expression ameliorates HOD by regulating the crosstalk between the liver and bone.

Our studies add to the knowledge of a crucial liver-bone axis in maintaining the metabolic homeostasis of the body (Ehnert et al., 2019; Nussler et al., 2014; Wang et al., 2015). As an important metabolic organ, the liver plays a significant role in the regulation of the brain and gut (Darshan and Anderson, 2007; Hamoud et al., 2018; Liang et al., 2014). Moreover, recent reports have shown that the bone is an important metabolic organ, releasing osteocalcin or other factors to regulate the periphery tissues (DiGirolamo et al., 2012; Fukumoto and Martin, 2009; Su et al., 2019). However, little is known about the pattern of regulation between the bone and the liver. It has been shown that liver-derived IGFBP1 can accelerate bone resorption through binding to the integrin β1 receptor in osteoclasts (Wang et al., 2015).

(H) Filipin III staining of intracellular cholesterol of primary osteoblasts treated with rLCAT for 24 h (scale bar, 50 μm) (1 technical replicate of 3 biological replicates per group).
(I–N) qRT-PCR of relative osteoblast marker gene (*Runx2*, *Sp7*, *Alp*, *Col1a2*, *Ocn*, and *Spp1*) mRNA levels of the groups indicated, with the level in the PBS group arbitrarily set to 1 (1 technical replicate of n = 4–6 biological replicates per group).
*p < 0.05, **p < 0.01, ***p < 0.001; NS, no significant difference. Two-way ANOVA followed by Tukey's post-test for multiple comparisons (B–G and I–N). Data are represented as mean ± SEM.
See also Figures S5 and S6.

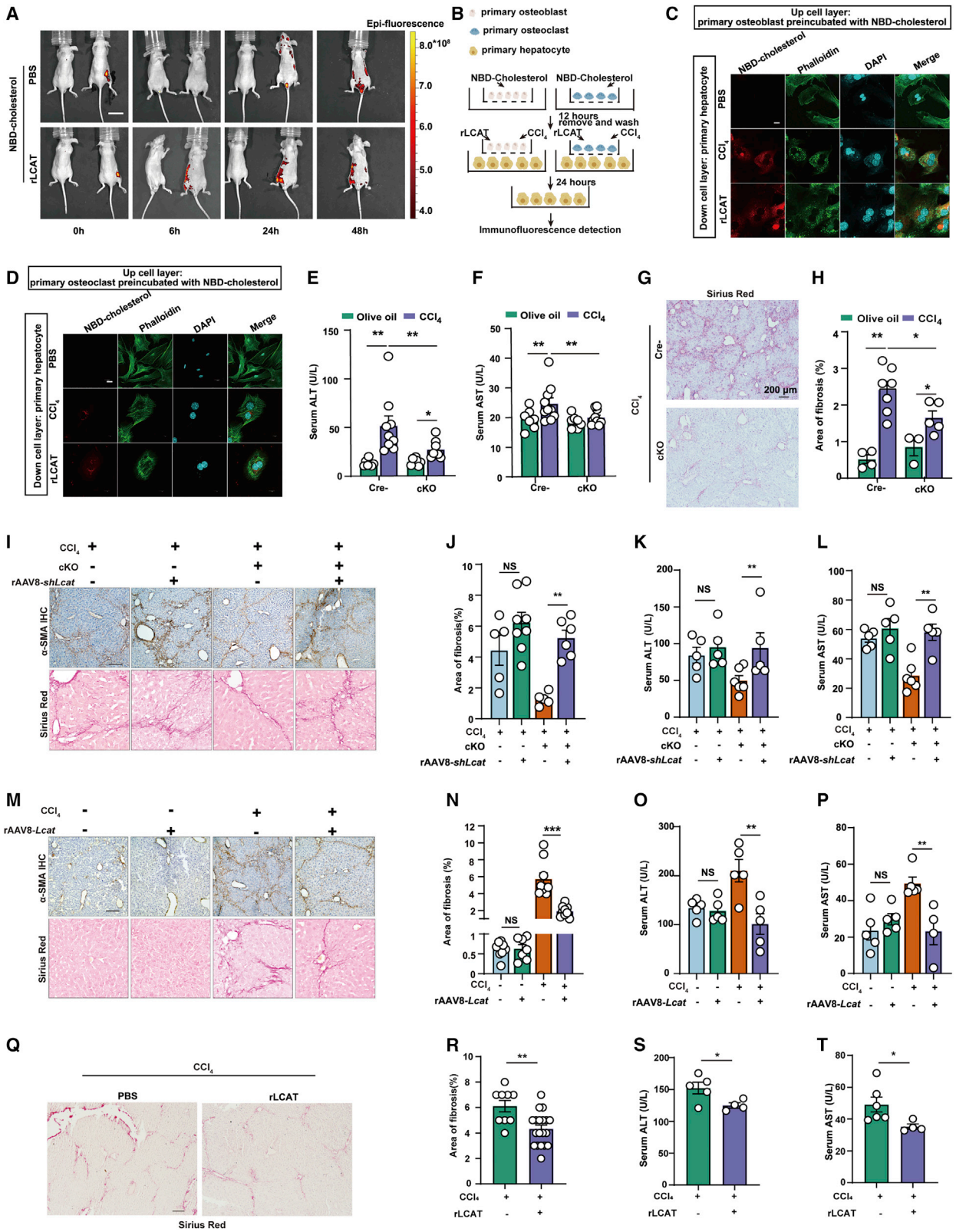

Figure 7. LCAT promotes liver recovery in HOD by promoting reverse cholesterol transport

(A) *In vivo* fluorescence images of NBD-cholesterol translocation from bone marrow in nude mice treated with or without rLCAT.

(B) Schematic diagram illustrating the design of the co-culture experiments.

(legend continued on next page)

Other studies focusing on VitD or other factors also found a communication between the bone and liver (Barbu et al., 2017). All these findings point to a liver-bone axis, and our findings support this concept further. Here, we found that liver injury increases bone resorption and inhibits bone formation to accelerate bone loss. Our proteomic analysis reveals that a large number of proteins were changed in the liver in individuals with HOD, most of which are involved in energy metabolisms. But specifically, we find that deletion of *PP2Acα*, a key phosphatase, in the liver can alleviate the bone loss induced by liver injury by increasing the viability of osteoblasts and inhibiting osteoclast maturation. Meanwhile, our studies also found that hepatocyte-specific PP2Acα deficiency in mice is associated with reduced liver injury after CCl_4 injury, mediated by an elevation in LCAT and likely due to reverse transport of cholesterol from the bone to the liver, further supporting the notion of a liver-bone crosstalk.

LCAT was originally discovered as a transferase of unsaturated FAs of lecithin at C2 sites in HDL to free cholesterol to generate the lysolecithin and cholesterol esters (Saeedi et al., 2015). Canonical evidence suggests that LCAT can maintain the unesterified cholesterol gradient between the cell membrane and extracellular acceptors, which contributes to a continuous efflux of cholesterol from periphery tissue to the circulation to accelerate reverse cholesterol transport (Obanda et al., 2016; Tanigawa et al., 2009). Notably, in this study, we discover that LCAT is a hepatokine and that its reduced expression mediates a defect in the liver-bone axis during HOD progression. Upon CCl_4-induced liver injury, liver-specific KO of *PP2Acα* promotes LCAT expression from liver. This result indicates that the liver can specifically secrete LCAT to regulate peripheral tissues (Warden et al., 1989). Our loss-of-function and gain-of-function studies further indicate that LCAT increases osteoblast viability while inhibiting osteoclast maturation, thus alleviating bone loss in our HOD mouse model. Compared to previous findings that LCAT serves as a canonical metabolic enzyme to regulate the levels of free cholesterol in the vascular system and correlates with the morbidity of atherosclerosis and fish-eye disease (Saeedi et al., 2015), our findings identify a novel role of LCAT—namely, as a mediator of proper bone and liver function, with defects in both tissues when its levels are suppressed.

Clinical studies have shown that hyperlipidemia may increase the risk of bone loss via regulation of osteoclast bone resorption and osteoblast bone formation (You et al., 2011). It has been reported that the Wnt-Lrp5 pathway could regulate FA utilization in osteoblasts through activation of β-catenin to induce the expression of key enzymes required for FA β-oxidation (Little-Letsinger et al., 2020). In contrast, free FAs inhibit osteoclastogenesis by activating peroxisome proliferator-activated receptors through inhibition of RANKL signaling (Kim et al., 2021). The cellular cholesterol may have an opposite effect in regulation of osteoblast and osteoclast functions (Yin et al., 2019). Free cholesterol may inhibit BMP2 to attenuate the expression of *Runx2*, *Alp*, and *Col1a1* in osteoblasts leading to inhibition of osteoblast differentiation (You et al., 2011). In contrast, depletion of cellular cholesterol prevents RANKL- or CSF-1-induced osteoclast formation (Luegmayr et al., 2004). Consistent with previous reports, our serum proteomic analysis from the *PP2Acα* cKO mice reveals significant changes in cholesterol metabolism, such as reverse cholesterol transport, cholesterol efflux, etc. Our findings suggest that cholesterol metabolism plays a potential role in the imbalance of the liver-bone axis induced by LCAT deficiency in HOD. Further, we demonstrate that liver-derived LCAT significantly inhibited osteoclast maturation through accelerating cholesterol efflux. Our results confirm the inhibition of osteoclast viability through disturbing the transcription of ERRα after acceleration of the cholesterol efflux (Wei et al., 2016). These results indicate that LCAT can inhibit the maturation of osteoclasts through accelerating the cholesterol efflux and the ERRα pathway. These findings are consistent with the previous report that the ligand activation of ERRα can be induced by cholesterol (Wei et al., 2016). Meanwhile, we also find that LCAT can regulate intracellular cholesterol transport to prevent cholesterol overloading and increase the viability of osteoblasts, which may be associated with ERRα activity (Yin et al., 2019). It has been reported that exogenous cholesterol inhibits osteoblast differentiation and that the physiological levels of endogenous cholesterol are essential for bone marrow stem cell osteogenesis (Li et al., 2019). These findings suggest that the effects of cholesterol on osteoblasts and cholesterol regulation patterns are complicated. Our results also suggest a new mechanism by which intracellular cholesterol may regulate osteoblast viability through affecting ERRα activity.

(C and D) Representative images of primary hepatocytes (determined by NBD-cholesterol IF [red] and Phalloidin IF [green]; DAPI was used for nuclear staining). Treatment of PBS or rLCAT or CCl_4 from primary osteoblasts (C) or primary osteoclasts (D) to hepatocytes in the co-culture system of primary hepatocytes (lower layers) (scale bar, 50 μm) (1 technical replicate of n = 9–14 biological replicates per group).
(E and F) Serum ALT and AST levels in *PP2Acα* cKO and Cre^- control mice with CCl_4 treatment (1 technical replicate of n = 7–10 biological replicates per group).
(G and H) Representative images of liver fibrosis (scale bar, 200 μm) and quantification of Sirius red staining-positive areas in the liver of *PP2Acα* cKO and Cre^- control mice with CCl_4 induction. Olive oil was used as a control (1 technical replicate of n = 3–7 biological replicates per group, 7 areas per mouse were analyzed).
(I–L) Extent of fibrosis (determined by Sirius red staining [I, upper] and α-SMA IHC [I, bottom] and Sirius red staining quantitation [J]) (1 technical replicate of n = 5–8 biological replicates per group, 7 areas per mouse were analyzed) (scale bar, 100 μm) and liver injury (determined by serum ALT and AST levels; K and L) in *PP2Acα* cKO and Cre^- control mice with rAAV8-*shLcat* injection (1 technical replicate of n = 5–6 biological replicates per group).
(M–P) Extent of fibrosis (determined by Sirius red staining [M, upper] and α-SMA IHC [M, bottom] and Sirius red staining quantitation [N]) (1 technical replicate of n = 7–9 biological replicates per group, 7 areas per mouse were analyzed) (scale bar, 100 μm) and liver injury (determined by serum ALT and AST levels; O and P) in *PP2Acα* cKO and Cre^- control mice with rAAV8-*Lcat* injection (1 technical replicate of n = 4–5 biological replicates per group).
(Q–T) Extent of fibrosis (determined by Sirius red staining [Q] [scale bar, 50 μm] and its quantitation [R]) (CCl_4, n = 9; CCl_4 + rLCAT, n = 19; 7 areas per mouse were analyzed) and liver injury (determined by serum ALT and AST levels; S and T) in CCl_4-injured mice after tail vein injection with rLCAT or carrier (PBS) (1 technical replicate of n = 4–5 biological replicates per group).
$^*p < 0.05$, $^{**}p < 0.01$, $^{***}p < 0.001$; NS, no significant difference. Two-way ANOVA followed by Tukey's post-test for multiple comparisons (E, F, H, J–L, and N–P) and two-tailed Student's unpaired t test analysis (R–T). Data are represented as mean ± SEM.
See also Figure S7.

Phosphorylation is one of the basic mechanisms that modifies protein structure and function (Blom et al., 1999). PP2A is an important phosphatase in the body, which regulates the phosphorylation/dephosphorylation levels of more than 90% of proteins in eukaryotes (Eichhorn et al., 2009). In fact, PP2A not only maintains intracellular metabolic stability, but also regulates protein secretion to maintain inter-organ stability. It has been shown that inhibition of the expression of PP2Acα in nerve cells could significantly reduce the secretion of BDNF and stabilize metabolism in other organs (Atasoy et al., 2017). However, the role of PP2A-mediated phosphorylation in the process of hepatic osteopathy is unclear. In our study, the expression of LCAT significantly increases in the hepatocyte-specific *PP2Acα* KO mice after CCL_4-induced liver injury, suggesting that the expression of LCAT is involved in the regulatory mechanism of PP2A-mediated phosphorylation modification. After bioinformation analysis, we find that the transcription factor, USF1, may play an important role in the process of LCAT expression, and the phosphorylation level at the Thr153 site in USF1 is significantly increased in *PP2Acα*-deficient cells after CCl_4 injury. Our further studies show that the increase in p-USF1 could significantly increase the luciferase activity of LCAT. This result is consistent with previous observations that the promotion of phosphorylation of USF1 at Thr153 could increase tyrosinase gene expression (Galibert et al., 2001).

Previous studies identify a number of biomarkers in the early diagnosis of osteoporosis or liver injury; however, none of them have been successfully utilized in the diagnosis of HOD (Barbu et al., 2017; Eastell et al., 2016). Recent studies reveal that almost 75% of individuals with chronic liver disease suffer from bone loss with an increased fracture risk (Nussler et al., 2014). But the key hepatokines correlating with HOD severity have not been identified. In the present study, we use a proteomic analysis of serum and tissues to construct a database of HOD. We not only find that changes of a liver-bone axis can be affected by the level of PP2Acα in the liver, but also demonstrate that LCAT can serve as a key regulator to impact the process of HOD. Thus, it is conceivable that testing for levels of liver PP2Acα and/or serum levels of LCAT can serve as a useful biomarker to determine the presence of HOD, its severity, or its progression. Likewise, based on our results here we propose that this pathway can go beyond being simply a biomarker but also serve as a therapeutic target to ameliorate both liver injury and bone loss in HOD progression.

Limitations of study

However, our studies also have some limitations. First, CCl_4 cannot fully induce chronic liver injury. Although it has been reported that CCl_4 can induce the mouse model of HOD, the etiology of chronic liver injury is mostly caused by hepatitis B virus infection, alcohol and/or drug use, or primary or secondary forms of cholestasis. Thus, the CCl_4-induced mouse model of chronic liver injury only exhibits part of the clinical pathological phenotypes (Barbu et al., 2017; López-Larramona et al., 2011). Thus, evaluation of PP2Acα levels and LCAT expression should be evaluated in other mouse models of chronic liver injury, as well as in more clinical samples with a better-defined etiology of HOD. Our studies also suggest that future research needs to focus on the evaluation of lipid metabolism and energy metabolism in individuals with HOD. Also, the study of LCAT on bone metabolism is currently limited to the regulation of cholesterol metabolism in osteoblasts and osteoclasts, and the target of LCAT needs to be further defined. Finally, the upstream mechanism to explain why PP2Acα expression is elevated in HOD needs to be determined.

STAR★METHODS

Detailed methods are provided in the online version of this paper and include the following:

- KEY RESOURCES TABLE
- RESOURCE AVAILABILITY
  - Lead contact
  - Materials availability
  - Data and code availability
- EXPERIMENTAL MODEL AND SUBJECT DETAILS
  - Mouse model
  - Human samples
  - Cell culture
- METHOD DETAILS
  - Design and production of rAAV8-*Lcat* and rAAV8-*shLcat*
  - Protein isolation, digestion, and labeling with iTRAQ reagents
  - LC-MS/MS Analysis and data analysis
  - Bioinformatics analysis
  - ELISA
  - Protein extraction and western blot detection
  - RNA extraction, Reverse Transcription and Real-Time PCR
  - Micro-CT analysis
  - Histological analysis
  - LCAT activity assay
  - Recombinant LCAT protein treatment
  - LCAT inhibitor treatment
  - TRAP staining
  - ALP staining
  - Sirius red staining
  - Nile red staining
  - Filipin III staining
  - Calcein staining and analysis
  - Co-immunoprecipitation assay
  - Cholesterol transplantation and *in vivo* imaging analysis
  - Dual luciferase reporter assay
- QUANTIFICATION AND STATISTICAL ANALYSIS

SUPPLEMENTAL INFORMATION

Supplemental information can be found online at https://doi.org/10.1016/j.cmet.2022.02.006.

ACKNOWLEDGMENTS

The research was supported by the National Natural Science Foundation of China (NSFC) (32071145 and 31771572), Natural Science Foundation of Jiangsu Province (BK20191356), Six Talent Peaks Project in Jiangsu Province (yy-014), Qin Lan Project of Jiangsu Province (KY520R202025), the Key R&D

Program of Jiangsu Province (BE2017708), NSFC Key Program (81730067 and 82030067), NSFC International (Regional) Collaboration Program (82161160342), Major Project of NSFC (81991514), Jiangsu Provincial Key Medical Center Foundation, Jiangsu Provincial Medical Outstanding Talent Foundation, Jiangsu Provincial Medical Youth Talent Foundation and Jiangsu Provincial Key Medical Talent Foundation, and the Fundamental Research Funds for the Central Universities (14380493 and 14380494).

AUTHOR CONTRIBUTIONS

Q.J., B.X., and C.-J.L. conceived and designed the work; K.L. and T.-S.S. obtained the data; S.-Y.S., Y.S., H.-L.G., J.W., and D.C. analyzed the data; Q.J. and B.X. provided funding support; K.L. and T.-S.S. drafted the manuscript; and B.X., D.C., X.G., H.-X.J., W.W., Y.C., and X.L. revised the manuscript.

DECLARATION OF INTERESTS

The authors declare no competing interests.

Received: May 7, 2021
Revised: November 26, 2021
Accepted: February 8, 2022
Published: March 1, 2022

REFERENCES

Amarasekara, D.S., Yun, H., Kim, S., Lee, N., Kim, H., and Rho, J. (2018). Regulation of osteoclast differentiation by cytokine networks. Immune Netw. *18*, e8.

Amini-Bavil-Olyaee, S., Choi, Y.J., Lee, J.H., Shi, M., Huang, I.C., Farzan, M., and Jung, J.U. (2013). The antiviral effector IFITM3 disrupts intracellular cholesterol homeostasis to block viral entry. Cell Host Microbe *13*, 452–464.

Atasoy, I.L., Dursun, E., Gezen-Ak, D., Metin-Armağan, D., Öztürk, M., and Yılmazer, S. (2017). Both secreted and the cellular levels of BDNF attenuated due to tau hyperphosphorylation in primary cultures of cortical neurons. J. Chem. Neuroanat. *80*, 19–26.

Barbu, E.C., Chiţu-Tiţu, C.E., Lazăr, M., Olariu, C., Bojincă, M., Ionescu, R.A., Ion, D.A., and Bădărău, I.A. (2017). Hepatic osteodystrophy: a global (re)view of the problem. Acta Clin. Croat. *56*, 512–525.

Baskaran, R., and Velmurugan, B.K. (2018). Protein phosphatase 2A as therapeutic targets in various disease models. Life Sci. *210*, 40–46.

Blom, N., Gammeltoft, S., and Brunak, S. (1999). Sequence and structure-based prediction of eukaryotic protein phosphorylation sites. J. Mol. Biol. *294*, 1351–1362.

Dandri, M., Burda, M.R., Török, E., Pollok, J.M., Iwanska, A., Sommer, G., Rogiers, X., Rogler, C.E., Gupta, S., Will, H., et al. (2001). Repopulation of mouse liver with human hepatocytes and in vivo infection with hepatitis B virus. Hepatology *33*, 981–988.

Darshan, D., and Anderson, G.J. (2007). Liver-gut axis in the regulation of iron homeostasis. World J. Gastroenterol. *13*, 4737–4745.

DiGirolamo, D.J., Clemens, T.L., and Kousteni, S. (2012). The skeleton as an endocrine organ. Nat. Rev. Rheumatol. *8*, 674–683.

Eastell, R., O'Neill, T.W., Hofbauer, L.C., Langdahl, B., Reid, I.R., Gold, D.T., and Cummings, S.R. (2016). Postmenopausal osteoporosis. Nat. Rev. Dis. Primers *2*, 16069.

Ehnert, S., Aspera-Werz, R.H., Ruoß, M., Dooley, S., Hengstler, J.G., Nadalin, S., Relja, B., Badke, A., and Nussler, A.K. (2019). Hepatic osteodystrophy-molecular mechanisms proposed to favor its development. Int. J. Mol. Sci. *20*, 2555.

Eichhorn, P.J., Creyghton, M.P., and Bernards, R. (2009). Protein phosphatase 2A regulatory subunits and cancer. Biochim. Biophys. Acta *1795*, 1–15.

Fukumoto, S., and Martin, T.J. (2009). Bone as an endocrine organ. Trends Endocrinol. Metab. *20*, 230–236.

Galibert, M.D., Carreira, S., and Goding, C.R. (2001). The Usf-1 transcription factor is a novel target for the stress-responsive p38 kinase and mediates UV-induced tyrosinase expression. EMBO J. *20*, 5022–5031.

Gu, P., Qi, X., Zhou, Y., Wang, Y., and Gao, X. (2012). Generation of Ppp2Ca and Ppp2Cb conditional null alleles in mouse. Genesis *50*, 429–436.

Guarino, M., Loperto, I., Camera, S., Cossiga, V., Di Somma, C., Colao, A., Caporaso, N., and Morisco, F. (2016). Osteoporosis across chronic liver disease. Osteoporos. Int. *27*, 1967–1977.

Hamoud, A.R., Weaver, L., Stec, D.E., and Hinds, T.D., Jr. (2018). Bilirubin in the liver-gut signaling axis. Trends Endocrinol. Metab. *29*, 140–150.

Han, Y., You, X., Xing, W., Zhang, Z., and Zou, W. (2018). Paracrine and endocrine actions of bone-the functions of secretory proteins from osteoblasts, osteocytes, and osteoclasts. Bone Res. *6*, 16.

Handzlik-Orlik, G., Holecki, M., Wilczyński, K., and Duława, J. (2016). Osteoporosis in liver disease: pathogenesis and management. Ther. Adv. Endocrinol. Metab. *7*, 128–135.

Humphrey, S.J., James, D.E., and Mann, M. (2015). Protein phosphorylation: a major switch mechanism for metabolic regulation. Trends Endocrinol. Metab. *26*, 676–687.

Karner, C.M., Lee, S.Y., and Long, F. (2017). Bmp induces osteoblast differentiation through both Smad4 and mTORC1 signaling. Mol. Cell. Biol. *37*, e00253-16.

Kim, S.P., Frey, J.L., Li, Z., Kushwaha, P., Zoch, M.L., Tomlinson, R.E., Da, H., Aja, S., Noh, H.L., Kim, J.K., et al. (2017). Sclerostin influences body composition by regulating catabolic and anabolic metabolism in adipocytes. Proc. Natl. Acad. Sci. USA *114*, E11238–E11247.

Kim, H., Oh, B., and Park-Min, K.H. (2021). Regulation of osteoclast differentiation and activity by lipid metabolism. Cells *10*, 89.

Lai, S.S., Zhao, D.D., Cao, P., Lu, K., Luo, O.Y., Chen, W.B., Liu, J., Jiang, E.Z., Yu, Z.H., Lee, G., et al. (2016). PP2Acα positively regulates the termination of liver regeneration in mice through the AKT/GSK3β/Cyclin D1 pathway. J. Hepatol. *64*, 352–360.

Lee, N.K., Sowa, H., Hinoi, E., Ferron, M., Ahn, J.D., Confavreux, C., Dacquin, R., Mee, P.J., McKee, M.D., Jung, D.Y., et al. (2007). Endocrine regulation of energy metabolism by the skeleton. Cell *130*, 456–469.

Lei, M., Wang, X., Ke, Y., and Solaro, R.J. (2015). Regulation of Ca(2+) transient by PP2A in normal and failing heart. Front. Physiol. *6*, 13.

Li, K., Xiu, C., Zhou, Q., Ni, L., Du, J., Gong, T., Li, M., Saijilafu, Yang, H., and Chen, J. (2019). A dual role of cholesterol in osteogenic differentiation of bone marrow stromal cells. J. Cell. Physiol. *234*, 2058–2066.

Liang, Q., Zhong, L., Zhang, J., Wang, Y., Bornstein, S.R., Triggle, C.R., Ding, H., Lam, K.S., and Xu, A. (2014). FGF21 maintains glucose homeostasis by mediating the cross talk between liver and brain during prolonged fasting. Diabetes *63*, 4064–4075.

Little-Letsinger, S.E., Pagnotti, G.M., McGrath, C., and Styner, M. (2020). Exercise and diet: uncovering prospective mediators of skeletal fragility in bone and marrow adipose tissue. Curr. Osteoporos. Rep. *18*, 774–789.

López-Larramona, G., Lucendo, A.J., González-Castillo, S., and Tenias, J.M. (2011). Hepatic osteodystrophy: an important matter for consideration in chronic liver disease. World J. Hepatol. *3*, 300–307.

Lu, N., Liu, Y., Tang, A., Chen, L., Miao, D., and Yuan, X. (2015). Hepatocyte-specific ablation of PP2A catalytic subunit α attenuates liver fibrosis progression via TGF-β1/Smad signaling. BioMed Res. Int. *2015*, 794862.

Luegmayr, E., Glantschnig, H., Wesolowski, G.A., Gentile, M.A., Fisher, J.E., Rodan, G.A., and Reszka, A.A. (2004). Osteoclast formation, survival and morphology are highly dependent on exogenous cholesterol/lipoproteins. Cell Death Differ. *11* (*Suppl 1*), S108–S118.

Maxfield, F.R., and Wüstner, D. (2012). Analysis of cholesterol trafficking with fluorescent probes. Methods Cell Biol. *108*, 367–393.

Mosialou, I., Shikhel, S., Liu, J.M., Maurizi, A., Luo, N., He, Z., Huang, Y., Zong, H., Friedman, R.A., Barasch, J., et al. (2017). MC4R-dependent suppression of appetite by bone-derived lipocalin 2. Nature *543*, 385–390.

Nussler, A.K., Wildemann, B., Freude, T., Litzka, C., Soldo, P., Friess, H., Hammad, S., Hengstler, J.G., Braun, K.F., Trak-Smayra, V., et al. (2014). Chronic CCl4 intoxication causes liver and bone damage similar to the human pathology of hepatic osteodystrophy: a mouse model to analyse the liver-bone axis. Arch. Toxicol. *88*, 997–1006.

Obanda, D.N., Ribnicky, D., Yu, Y., Stephens, J., and Cefalu, W.T. (2016). An extract of Urtica dioica L. mitigates obesity induced insulin resistance in mice skeletal muscle via protein phosphatase 2A (PP2A). Sci. Rep. *6*, 22222.

Parfitt, A.M., Drezner, M.K., Glorieux, F.H., Kanis, J.A., Malluche, H., Meunier, P.J., Ott, S.M., and Recker, R.R. (1987). Bone histomorphometry: standardization of nomenclature, symbols, and units. Report of the ASBMR Histomorphometry Nomenclature Committee. J. Bone Miner. Res. *2*, 595–610.

Rhee, Y., Kim, W.J., Han, K.J., Lim, S.K., and Kim, S.H. (2014). Effect of liver dysfunction on circulating sclerostin. J. Bone Miner. Metab. *32*, 545–549.

Roman-Garcia, P., Quiros-Gonzalez, I., Mottram, L., Lieben, L., Sharan, K., Wangwiwatsin, A., Tubio, J., Lewis, K., Wilkinson, D., Santhanam, B., et al. (2014). Vitamin B_{12}-dependent taurine synthesis regulates growth and bone mass. J. Clin. Invest. *124*, 2988–3002.

Saeedi, R., Li, M., and Frohlich, J. (2015). A review on lecithin:cholesterol acyltransferase deficiency. Clin. Biochem. *48*, 472–475.

Schmidt, T., Schwinge, D., Rolvien, T., Jeschke, A., Schmidt, C., Neven, M., Butscheidt, S., Kriz, M., Kunzmann, L., Mussawy, H., et al. (2019). Th17 cell frequency is associated with low bone mass in primary sclerosing cholangitis. J. Hepatol. *70*, 941–953.

Shergill, R., Syed, W., Rizvi, S.A., and Singh, I. (2018). Nutritional support in chronic liver disease and cirrhotics. World J. Hepatol. *10*, 685–694.

Song, W., Wang, W., Wang, Y., Dou, L., Chen, L., and Yan, X. (2015). Characterization of fluorescent NBD-cholesterol efflux in THP-1-derived macrophages. Mol. Med. Rep. *12*, 5989–5996.

Su, N., Yang, J., Xie, Y., Du, X., Chen, H., Zhou, H., and Chen, L. (2019). Bone function, dysfunction and its role in diseases including critical illness. Int. J. Biol. Sci. *15*, 776–787.

Tanigawa, H., Billheimer, J.T., Tohyama, J., Fuki, I.V., Ng, D.S., Rothblat, G.H., and Rader, D.J. (2009). Lecithin: cholesterol acyltransferase expression has minimal effects on macrophage reverse cholesterol transport in vivo. Circulation *120*, 160–169.

Uretmen, S., Gol, M., Cimrin, D., and Irmak, E. (2005). Effects of chronic liver disease on bone mineral density and bone metabolism markers in postmenopausal women. Eur. J. Obstet. Gynecol. Reprod. Biol. *123*, 67–71.

van der Velde, A.E. (2010). Reverse cholesterol transport: from classical view to new insights. World J. Gastroenterol. *16*, 5908–5915.

Wang, P.Y., Caspi, L., Lam, C.K., Chari, M., Li, X., Light, P.E., Gutierrez-Juarez, R., Ang, M., Schwartz, G.J., and Lam, T.K. (2008). Upper intestinal lipids trigger a gut-brain-liver axis to regulate glucose production. Nature *452*, 1012–1016.

Wang, X., Wei, W., Krzeszinski, J.Y., Wang, Y., and Wan, Y. (2015). A liver-bone endocrine relay by IGFBP1 promotes osteoclastogenesis and mediates FGF21-induced bone resorption. Cell Metab. *22*, 811–824.

Warden, C.H., Langner, C.A., Gordon, J.I., Taylor, B.A., McLean, J.W., and Lusis, A.J. (1989). Tissue-specific expression, developmental regulation, and chromosomal mapping of the lecithin: cholesterol acyltransferase gene. Evidence for expression in brain and testes as well as liver. J. Biol. Chem. *264*, 21573–21581.

Wei, W., Wang, X., Yang, M., Smith, L.C., Dechow, P.C., Sonoda, J., Evans, R.M., and Wan, Y. (2010). PGC1beta mediates PPARgamma activation of osteoclastogenesis and rosiglitazone-induced bone loss. Cell Metab. *11*, 503–516.

Wei, J., Shimazu, J., Makinistoglu, M.P., Maurizi, A., Kajimura, D., Zong, H., Takarada, T., Lezaki, T., Pessin, J.E., Hinoi, E., and Karsenty, G. (2015). Glucose uptake and Runx2 synergize to orchestrate osteoblast differentiation and bone formation. Cell *161*, 1576–1591.

Wei, W., Schwaid, A.G., Wang, X., Wang, X., Chen, S., Chu, Q., Saghatelian, A., and Wan, Y. (2016). Ligand activation of ERRα by cholesterol mediates statin and bisphosphonate effects. Cell Metab. *23*, 479–491.

Xian, L., Hou, S., Huang, Z., Tang, A., Shi, P., Wang, Q., Song, A., Jiang, S., Lin, Z., Guo, S., and Gao, X. (2015). Liver-specific deletion of Ppp2cα enhances glucose metabolism and insulin sensitivity. Aging (Albany N.Y.) *7*, 223–232.

Yin, W., Li, Z., and Zhang, W. (2019). Modulation of bone and marrow niche by cholesterol. Nutrients *11*, 1394.

You, L., Sheng, Z.Y., Tang, C.L., Chen, L., Pan, L., and Chen, J.Y. (2011). High cholesterol diet increases osteoporosis risk via inhibiting bone formation in rats. Acta Pharmacol. Sin. *32*, 1498–1504.

STAR★METHODS

KEY RESOURCES TABLE

REAGENT or RESOURCE	SOURCE	IDENTIFIER
Antibodies		
Anti-PP2Acα	Abcam	RRID: AB_777385, AB_779044
Anti-Osteocalcin	Abcam	RRID: AB_10675660
Anti-LCAT	Abcam	RRID: AB_2281243
Anti-USF1	Santa Cruz	RRID: AB_2885177
Anti-p(Ser/Thr) Phe	Abcam	RRID: AB_443891
Anti-pUSF1(Thr153)	Thermofisher	RRID: AB_2662685
Anti-Collagen 1	Abclonal	RRID: AB_2766539
Anti-Runx2	Abcam	RRID: AB_2713945
Anti-PCNA	Santa Cruz	RRID: AB_628110
Anti-Gapdh	Abclonal	RRID: AB_2736879
Anti-β-actin	Abclonal	RRID: AB_2768234
Anti-Ctsk	Abcam	RRID: AB_2885178
Anti-Trap	Abcam	RRID: AB_11131206
Anti-α-tublin	Abclonal	RRID: AB_2768341
Anti-HRP goat anti-rabbit	Abclonal	RRID: AB_2769854
Anti-HRP goat anti-mouse	Abclonal	RRID: AB_2769851
Anti-goat anti-mouse IgG Alexa Fluor 594	Invitrogen	RRID: AB_2534091
Anti-goat anti-rabbit IgG Alexa Fluor 488	Invitrogen	RRID: AB_2576217
Chemicals, peptides, and recombinant proteins		
Paraformaldehyde	Aladdin	Cat # C104190
Dexamethasone	Sigma-Aldrich	Cat # D2915
Ascorbic acid	Sigma-Aldrich	Cat # A4544
b-glycerophosphate	Sigma-Aldrich	Cat # G9422
ITS liquid media supplement (100 ×)	Sigma-Aldrich	Cat # I3146
Calcein	Sigma-Aldrich	Cat # C0875
Recombinant mouse M-CSF protein	R&D Systems	Cat # 416-ML
Recombinant mouse TRANCE/RANK L/ TNFSF11	R&D Systems	Cat # 462-TEC
Nile Red	Sigma-Aldrich	Cat # 72485
DAPI, 4′,6-diamidino-2-phenylindole	Sigma-Aldrich	Cat # MBD0020
Filipin III	Sigma-Aldrich	Cat # SAE0087
NBD cholesterol	Invitrogen	Cat # N1148
Isoflurane	RWD Life Science	Cat # R510-22
Critical commercial assays		
Clarity ECL substrate	BioRad	Cat # 1705060
TGX FastCast Acrylamide Solutions	BioRad	Cat # 1610172
RNA-Quick Purification Kit	Esunbio	Cat # ES-RN001
Acid Phosphatase, Leukocyte (TRAP) Kit	Sigma-Aldrich	Cat # 387A
Alkaline phosphatase stain Kit	Keygen	Cat # KGA353
Cross Linked C-Telopeptide Of Type I Collagen (CTXI) Elisa Kit	Cloud-Clone	Cat # CEA665Mu
Osteocalcin (Ocn) Elisa Kit	Novus	Cat # NBP2-68151
Human LCAT Elisa Kit	Cloud-Clone	Cat # SEJ516Hu
Mouse LCAT Elisa Kit	Cloud-Clone	Cat # SEJ516Mum
LCAT Acitivity Assay Kit	Sigma-Aldrich	Cat # MAK107

(*Continued on next page*)

Continued		
REAGENT or RESOURCE	SOURCE	IDENTIFIER
Immunoaffinity Albumin & IgG Depletion Kit	Millipore	Cat # PROTIA
Deposited data		
Proteomics data	Mendeley.com	https://doi.org/10.17632/z53hvmtsg6.1
Raw Data	This paper	Data S1
Experimental models: Cell lines		
Mouse: RAW264.7	Genetimes	Cat #Sc-6003
Mouse: MC3T3-E1	Genetimes	Cat # CRL-2593
Mouse: AML12	Genetimes	Cat # CRL-2254
Experimental models: Organisms/strains		
Mouse: PP2Acα $^{fl/fl}$(B6/JGpt-Ppp2caem1Cflox/Gpt)	GemPharmatech	Stock No T018350
Mouse: ALB-Cre (B6/JGpt-H11em1Cin (Alb-iCre)/Gpt)	GemPharmatech	Stock No T003814
Mouse: C57BL/6 (Wt) mice	GemPharmatech	Stock No N000013
Mouse: BALB/c-Nude	GemPharmatech	Stock No D000521
Oligonucleotides		
Primer for mouse PP2Acα, see Table S3	GeneRay.Biotech	N/A
Primer for human PP2Acα, see Table S3	GeneRay.Biotech	N/A
Primer for mouse LCAT, see Table S3	GeneRay.Biotech	N/A
Primer for mouse Runx2, see Table S3	GeneRay.Biotech	N/A
Primer for mouse Alpl, see Table S3	GeneRay.Biotech	N/A
Primer for mouse Sp7, see Table S3	GeneRay.Biotech	N/A
Primer for mouse Ctsk, see Table S3	GeneRay.Biotech	N/A
Primer for mouse Oscar, see Table S3	GeneRay.Biotech	N/A
Primer for mouse Ocn, see Table S3	GeneRay.Biotech	N/A
Primer for mouse Trap, see Table S3	GeneRay.Biotech	N/A
Primer for mouse Idh3a, see Table S3	GeneRay.Biotech	N/A
Primer for mouse Vlcad, see Table S3	GeneRay.Biotech	N/A
Primer for mouse Aco2, see Table S3	GeneRay.Biotech	N/A
Primer for mouse Collagen I αII, see Table S3	GeneRay.Biotech	N/A
Primer for mouse osteopontin, see Table S3	GeneRay.Biotech	N/A
Primer for Human ADK, see Table S3	GeneRay.Biotech	N/A
Primer for Human AK2, see Table S3	GeneRay.Biotech	N/A
Primer for Human CAMK2D, see Table S3	GeneRay.Biotech	N/A
Primer for Human CMPK1, see Table S3	GeneRay.Biotech	N/A
Primer for Human CPPED1, see Table S3	GeneRay.Biotech	N/A
Primer for Human KHK, see Table S3	GeneRay.Biotech	N/A
Primer for Human NADK2, see Table S3	GeneRay.Biotech	N/A
Primer for Human NME2, see Table S3	GeneRay.Biotech	N/A
Primer for Human PCK1, see Table S3	GeneRay.Biotech	N/A
Primer for Human PCK2, see Table S3	GeneRay.Biotech	N/A
Primer for Human PFKL, see Table S3	GeneRay.Biotech	N/A
Primer for Human PGK1, see Table S3	GeneRay.Biotech	N/A
Primer for Human PGP, see Table S3	GeneRay.Biotech	N/A
Primer for Human PKLR, see Table S3	GeneRay.Biotech	N/A
Primer for Human PKM, see Table S3	GeneRay.Biotech	N/A
Primer for Human PPP3CA, see Table S3	GeneRay.Biotech	N/A
Primer for Human PRKAR1A, see Table S3	GeneRay.Biotech	N/A
Primer for Human SACM1L, see Table S3	GeneRay.Biotech	N/A

(*Continued on next page*)

Continued		
REAGENT or RESOURCE	SOURCE	IDENTIFIER
Primer for Human TKFC, see Table S3	GeneRay.Biotech	N/A
Software and algorithms		
ImageJ	https://imagej.nih.gov/ij/	N/A
Graphpad Prism 8 software	https://www.graphpad.com/	N/A
Other		
α-MEM	GIBCO	Cat # 12561-056
DMEM/F-12	GIBCO	Cat # 11320-033
DMEM	GIBCO	Cat # 11965-092
PowerTrack SYBR Green Master Mix	Thermofisher	Cat # A46109

RESOURCE AVAILABILITY

Lead contact

Further information and requests for resources and reagents should be directed to and will be fulfilled by the Lead Contact, Qing Jiang (qingj@nju.edu.cn).

Materials availability

All materials used in this study are either commercially available or obtained through collaboration, are available from the corresponding authors upon request.

Data and code availability

- Proteomics data are deposited in the Mendeley repository: https://doi.org/10.17632/z53hvmtsg6.1
- No new code has been generated in this study.
- Data S1 represents an Excel file containing the values that were used to create all the graphs in the paper, as well as a PDF file containing the full-length, unprocessed western blots. Any additional information required to reanalyze the data reported in this paper is available from the lead contact upon request.

EXPERIMENTAL MODEL AND SUBJECT DETAILS

Mouse model

All animals (PP2Acα-Floxed, ALB-Cre, BALB/c-Nude, C57BL/6 mice) used in this study were bought from Model Animal Research Centre of Nanjing University were bred and housed in a specific pathogen-free facility (SPF) in individually ventilated cages, 3 mice per cage, with health status checks every three months and kept with a 12-h light and 12-h dark (20:00–08:00) photoperiod and a controlled housing temperature at 22°C. All animals were fed a standard chow diet (SWS9102 or SFS9112 from Xie-Tong Biomedicine, Nanjing, China). The majority of subjects from the study are the result of in-house mating and littermate controls were used. Male and female mice from 12 weeks of age were imported into the facility to complete experimental groups. The PP2Acα-Floxed animals and mated with the mice expressed Alb-Cre to generate the PP2Acα$^{fl/fl}$ x Alb-Cre mice (Gu et al., 2012). Genotyping was performed by PCR analysis of DNA isolated from mouse tails. The following genotyping primers were used: Cre, forward primer (5′-GCCTGCATTACCGGTCGATGC-3′) and reverse primer (5′-CAGGGTGTTATAAGCAATCCC-3′); and Loxp, forward primer (5′-AAGTTACTGGCAGTGTGCCTTG-3′) and reverse primer (5′-TTATACCCTTCCTCATTCGCTCTGC-3′). RT-PCR was performed to detect the excision of exon 3-5 of Ppp2ca cDNA in adult mice. The wild-type variant is 877 bp, whereas the mutant variant is 451 bp.

For generating the hepatic osteodystrophy (HOD) model, the mice with 12-weeks of aged were treated with carbon tetrachloride (CCl_4) for 6 weeks (1 mL/kg body weight mixed with olive oil; 3 injections per week i.p.) according to the previous study (Nussler et al., 2014). After CCl_4 injection, the mice were sacrificed for obtaining the serum, liver and bone. All animals' protocols were reviewed and approved by the animal care committee of Drum Tower Hospital, Nanjing in accordance with institutional animal care and use committee guidelines.

Human samples

The human samples and data were collected from the Liver and Gallbladder Research Center of Drum Tower Hospital. Participants with hepatic hemangioma and liver cirrhosis who were willing to participate in the study were included. The patients did not have the following exclusion criteria: (1) use of corticosteroids within the last 3 months; (2) acute infection;(3) autoimmune disease; (4) the severe cardiovascular and cerebrovascular diseases. Before the surgery, the individuals' bone mineral density was detected by DXA and their blood samples were collected. The human liver tissue was collected during the surgery which was cut out for pathological

analysis. The study was conducted with the approval of the ethics committees of the Drum Tower Hospital (No.2021-192). Written informed consent was provided by all participants.

Cell culture

All cells were grown at 37°C in a 5% CO_2 humid atmosphere, and all growth medium were supplemented with 100 units/mL penicillin and 100 μg/mL streptomycin. The murine hepatic cell line, AML12 were maintained in Dulbecco's modified Eagle's medium (DMED) F12 (DMEM-F12) with 10% fetal bovine serum, which was added the 40 ng/mL dexamethasone and 1% ITS liquid media supplementary. The murine monocytic cell line RAW264.7 was cultured in DMEM supplemented with 10% fetal bovine serum. For osteoclastogenesis experiments, the recombinant RANKL protein was added at the concentration of 50 ng/mL. The murine osteoblast cell line, MC3T3-E1, was cultured in α-MEM 10% FBS. For osteoblastogenesis experiments, the growth media was supplemented with 10 nM dexamethasone, 50 μg/mL ascorbic acid and 10 mM β-glycerophospate.

Primary hepatocytes were isolated from the mouse liver used a modified two-step perfusion protocol. Briefly, 8-weeks-aged C57/b6 mice and *PP2Acα* cKO mice were perfused through Earle's balanced salt solution (EBSS) plus 5 mM EDTA. After that, the Hank's balanced salt solution (HBSS) was perfused which was supplemented with the 100 U/mL collagenase IV and trypsin inhibitors. Then the liver was dissociated into single cell suspension. After passed through the cell meshes, the cells were seeded on the collagen coated plate at the concentration of $0.2x10^6$ with αMEM.

Primary osteoblasts were isolated from the 5-day-old mouse calvarias as previous researches (Lee et al., 2007). Briefly, the calvarias were sacrificed by fast decapitation and cleared the skin and fiber texture. After that, the calvarias were incubated in PBS containing 1% trypsin and 4 mM EDTA at 37°C for two 10 min periods. The obtained supernatants were discarded. Subsequently, calvarias were digestion in PBS containing 200 U/mL collagenase II for 45 min. the supernatants were centrifugation and rinsed in PBS for two times. Then, cells were cultured in αMEM supplemented with 10% FBS. For osteoblastogenesis experiments, the growth media was supplemented with 10nM dexamethasone, 50 μg/mL ascorbic acid and 10 mM β-glycerophosphate.

Primary osteoclasts were isolated from the femur and tibia of 4-week-old mouse as previous researches reported. Briefly, the bone marrow cavity was flushed with cold PBS and pass through the cell meshes. The obtained supernatants were centrifugation and rinsed in PBS for two times. Then, the cell was cultured in αMEM supplemented with 10% FBS and 30 ng/mL M-CSF for proliferation. For osteoclastogenesis experiments, the recombinant RANKL protein was added at the concentration of 50 ng/mL.

METHOD DETAILS

Design and production of rAAV8-*Lcat* and rAAV8-*shLcat*

The shRNA of *Lcat* was constructed by OBiO Technology (Shanghai, China). The target sequence used against mouse *Lcat* was as follows: 5′-CCATCTGGCTGGATTTCAA-3′. The sequence of 5′- TTCTCCGAACGTGTCACGT-3′ was used as a control-shRNA. The *Lcat* shRNA sequence and control shRNA sequence were cloned into the pDKD-CMV-U6-shRNA vector for further packaging. The overexpression of *Lcat* plasmid and control plasmid was also constructed by OBiO Technology using pAdeno-MCMV-3Flag-IRES2 carrier. Further, the rAAV8 serotype was selected to construct the rAAV8-*Lcat* and -*shLcat*. The purified virus was diluted in sterile PBS. Each mouse received single tail vein injection of 2×10^{11} copies of rAAV8-*shLcat* or rAAV8-*Lcat*. 2 weeks after injection, the mice received CCl_4 treatment for 6 weeks (1 mL/kg body weight, mixed with olive oil; 3 injections per week, i.p. injection). The mice were sacrificed at indicated time and the serum, bone and liver tissues were harvested.

Protein isolation, digestion, and labeling with iTRAQ reagents

Human liver tissue samples were lysed in RIPA lysis buffer (50 mM Tris-HCl, 0.5% NP-40, 0.25% Na-deoxycholate, 1 mM EDTA and 1% Protease Inhibitor Cocktail, 1 mM PMSF, 1 mM NaVO3, 1 mM NaF, pH7.4), and broken by the ultrasonic wave for 10 min on ice, then following centrifugation at 12,000 rpm for 30 min to remove cell debris. The supernatant was collected. The protein concentration was determined with the BCA protein assay. Mice plasma were collected in 1.5 mL EP tubes and after standing for 2 h at room temperature, the plasma was centrifugation at 3000 rpm for 30 min and the supernatant was collected. The serum should be removed the albumin and IgG before proteomics analysis (Sigma-Aldrich) according to the manufacturers. The protein concentration was also determined with the BCA protein assay.

For on-filter digestion, an aliquot of total protein (50 μg) was diluted to 100 μL with 0.5 M TEAB, reduced with 5 mM TCEP for 1 h at 55°C and alkylated with 6.25 mM MMTS for 30 min at room temperature in darkness. The protein lysates were transferred to 10k Vivacon filter following centrifugation at less than 12000 rpm for 30 min to remove solvent, and washed 3 times with 0.5 M TEAB. Finally, trypsin was added onto the filter at 1:50 trypsin-to-protein mass ratio for the first digestion overnight and 1:100 trypsin-to-protein mass ratio for a second 4 h-digestion at 37°C.

The peptides were collected and labeled with iTRAQ Reagent-8 plex Multiplex Kit (AB Sciex UK Limited) according to the manufacturer's instructions. The samples and labeled marker were as follows: the HOD group samples were labeled with iTRAQ tag 113, iTRAQ tag 114, or iTRAQ tag 115, or iTRAQ tag 116 and the cirrhosis group samples were labeled with iTRAQ tag 117, iTRAQ tag 118, iTRAQ tag 119 or iTRAQ tag 121. All of the labeled samples were mixed with an equal amount. The labeled samples were fractionated using high-performance liquid chromatography (HPLC) system (SHIMADZU) using a Durashell C18 (5 μm, 100 Å, 4.6 × 250 mm). Finally, 12 fractions were collected.

LC-MS/MS Analysis and data analysis

Data acquisition was performed with a Triple TOF 5600 System (AB SCIEX, Concord, ON). Samples were chromatographed using a 90 min gradient from 2%–30% (mobile phase A 0.1% (v/v) formic acid, 5% (v/v) acetonitrile; mobile phase B 0.1% (v/v) formic acid, 95% (v/v) acetonitrile) after direct injection onto a 20 μm PicoFrit emitter (New Objective) packed to 12 cm with Magic C18 AQ 3 μm 120 Å stationary phase. MS1 spectra were collected in the range 350-1,500 m/z for 250 ms. The 20 most intense precursors with charge state 2-5 were selected for fragmentation, and MS2 spectra were collected in the range 50-2,000 m/z for 100 ms; precursor ions were excluded from reselection for 15 s.

The original MS/MS file data were submitted to ProteinPilot Software (version 4.5, AB Sciex) for data analysis. MS/MS data were searched against *Mus musculus* UniProt database (April 9, 2016, containing 50,943 sequences http://www.uniprot.org/proteomes/UP000000589). / Tandem mass spectra were searched against *Homo sapiens* UniProt database (April 9, 2016, containing 160,566 sequences, http://www.uniprot.org/proteomes/UP000005640) concatenated with reverse decoy database.

The following search parameters were used: the instrument was TripleTOF 5600, iTRAQ quantification, cysteine modified with MMTS; biological modifications were selected as ID focus, the Quantitate, trypsin digestion, Bias Correction and Background Correction was checked for protein quantification and normalization. For false discovery rate (FDR) calculation, an automatic decoy database search strategy was used to estimate FDR using the PSPEP (Proteomics System Performance Evaluation Pipeline Software) algorithm. Only proteins with at least two unique peptides were considered for further analysis. For protein abundance ratios measured using iTRAQ after normalization, we specifically used ratios with p value < 0.05, and only fold changes > 1.5 or < 0.667 were considered significant.

Bioinformatics analysis

The identified and differentially expressed proteins sequences were mapped with Gene Ontology Terms (https://david.ncifcrf.gov/). Pathway analyses were conducted using the Kyoto Encyclopedia of Genes and Genomes (KEGG) platform. The pathway enrichment statistics were performed by Fisher' s exact test, and those with a corrected p value < 0.05 were considered the most significant pathways.

ELISA

The concentration of serum CTX-1 from mice were measured with Cloud-Clone CTX-1 Elisa Kit (CEA665Mu) in 1:2 diluted serum samples. The serum osteocalcin of mice was measured with Novus Elisa Kit (NBP2-68151) in 1:2 diluted serum samples. The serum LCAT from mice and human were measured with Cloud-Clone Elisa Kit (SEJ516Hu and SEJ516Mum, respectively). The serum ALT and AST were measured with Jiancheng Kit (C009-2-1 and C010-2-1, respectively). All measures were done according to manufacturers' instructions.

Protein extraction and western blot detection

The samples of liver or cells was homogenized and incubated in RIPA buffer (Thermo, Prod # 89901) supplemented with 1mM PMSF, 1mM Na_3VO_4 and protease inhibitor. The homogenization buffer was centrifuged at 12000 g for 10 min. The supernatants were moved into another new centrifugal tubes. The sample buffer (5x, BOSTER) was added and warmed at 99°C for 5 min. Then, the samples were frozen in the −80°C refrigerator.

For western blot, the protein samples were subjected to SDS-PAGE using 10% gels (YAMEI, China). After separation, samples were electrotransferred onto a fit PVDF membrane (Merck Millipore) and blocked with blocking buffer (4% non-fat milk) for one h at room temperature. The primary antibodies of PP2Acα (1:1000), LCAT (1:500), USF-1 (1:500), p-USF-1 (Thr 153) (1:1000), Collagen I (1:1000), Runx2 (1:1000), β-actin (1:2000), p(Ser/Thr) Phe (1:1000), PCNA (1:1000), Ctsk (1:1000), *TRAP* (1:1000), α-Tubulin (1:2000) was added and incubated at 4°C for overnight. After washing with PBS-T (0.2% Tween 20), secondary antibodies (1:10000) were applied for 1 h at room temperature and washing with PBST again. Finally, the visualized analysis was used with Li-Cor Odyssey equip.

RNA extraction, Reverse Transcription and Real-Time PCR

The mRNA of tissues or cultured cell were extracted by adding the appropriate amount of RNAiso (Takara) according to the manufacturer's instructions. After homogenizing the samples at room temperature for 5 min, the chloroform of 0.2 volume of RNAiso was added and vortexed vigorously. After centrifuging at 12000 g for 5 min at 4°C, the supernatant was transferred to the new centrifuge tube. The same volume of isopropanol was added and centrifuged again as before. The pellet obtained was washed with equivalent amount of 75% ethanol for two times and ultimately resuspended in 30 μL DEPC-treated water. For reverse transcription, we added 4 μL of the cDNA synthesis mix (Takara) to 1 μg RNA per sample according to the manufacturer's instructions. Real-time PCR was done on the ABI Viia 7 (Thermo) with SYBR Green-based detection. the primer sequences were shown in the Supplemental Data. The results were collected using standard curve method and normalized to the β-Actin or GAPDH.

Micro-CT analysis

After the mice scarified, the left femurs were fixed in 4% formaldehyde overnight and washed by PBS before scanning. The MicroCT analysis was performed according to the previous researches in MicroCT scanner (SkyScan, Aarselaar). X-ray voltage and current were set at 80 kV and 80 μA, respectively, with a resolution of 18 μm per pixel. The region from 0.05 mm below the growth plate to 5%

of femoral length was selected for 3-dimensional histomorphometric analysis to determine cortical or trabecular bone mineral density (BMD), trabecular bone volume per tissue volume (BV/TV), trabecular number (Tb. N.), trabecular spacing (Tb. Sp.), and trabecular thickness (Tb. Th.).

Histological analysis

The right femurs were fixed in 4% formaldehyde overnight and decalcified in 5% EDTA in PBS for 2 weeks. The decalcified bone tissues were embedded in paraffin after dehydration and then cut into 7-μm-thick slices. The slices of bone were used for TRAP staining, IHC or IF staining. The liver tissues from both individuals and mice were fixed in 4% formaldehyde for 4 h and embedded in paraffin after dehydration. Then, the samples were cut into 7-μm-thick slices and used for the sirius red staining. The stained slices were then photographed using an Olympus BX51 phase contrast light microscope.

LCAT activity assay

The activity of rLCAT was detected by the LCAT Activity Assay Kit (Sigma-Aldrich). Briefly, different volume of rLCAT or PBS and 0.5 μL of substrate were combined into the well of polypropylene reaction plate, and bring to final volume of 100 μL with LCAT assay buffer. The plate was incubated for 2.5 h at 37°C. Then 200 μL of read reagent was added and mixed. 200 μL of reaction mixture was then transferred to a black fluorescence microplate. The increase in fluorescence of samples was detected by a fluorometer (Molecular Devices M3, USA) (λex = 340 nm) and the ratio (λem 470 nm/λem 390 nm) was determined. Briefly, the relative intensity of two distinct peaks, 390 nm and 470 nm (emission spectrum) depends on the concentrations of hydrolyzed or intact substrate present in the assay. After hydrolysis of the substrate by LCAT, the 390 nm peak is increased while the 470 nm peak is decreased.

Recombinant LCAT protein treatment

The mature C57b/L6 mice were injected the recombinant LCAT protein for 5 μg/kg body weight per mouse started from the first weeks of CCl_4 treatment. The recombinant LCAT was dissolved into 1% BSA-PBS buffer. The Ctrl group was administrated with 1% BSA-PBS buffer as the same volume compare to the Treatment group. After total 24 times of rLCAT injection three times a week, the mice were scarified for the further histopathological analysis.

LCAT inhibitor treatment

The mature *PP2Acα* cKO and WT mice were injected the 5,5′-dithio-bis (2-nitrobenzoic acid) (DTNB) for 3 μl/g body weight (100 μM DTNB) per mouse started from the second weeks of CCl_4 treatment. After total five times of DTNB injection once a week, the mice were scarified for the further histopathological analysis.

TRAP staining

Bone slices were dewaxed in xylene and rehydrated in diminishing concentrations of ethanol. The staining buffer was freshly prepared according to the manufacturer's instruction. Briefly, the equal amount of the Fast Garnet GBC base solution and sodium nitrite solution was mixed and added into the deionized water. The Naphthol AS-TR phosphate solution, the acetate solution and the tartrate solution were added into the water. The slices were incubated for 1 h. After washing the slices by PBS, the slices were sealed by glycerin, and photographed using an Olympus BX51 phase contrast light microscope. Moreover, the trap staining of cultured cells has the similar protocol including the staining solution preparation. But the cells were fixed with 4% formaldehyde for 10 min and washed by PBS. After then, the staining solution was added into the cells for trap staining.

ALP staining

The primary osteoblasts were cultured in α-MEM supplemented with 10 nM dexamethasone, 50 μg/mL ascorbic acid and 10 mM β-glycerophosphate for 7 days. After fixed with 4% formaldehyde for 10 min and washed with PBS, the cells were incubated in the working solution (A solution mixed with B solution) (KGA353, KeyGEN BioTECH) for 3 h at 37°C. The cells were then rinsed with water before being processed for imaging analysis.

Sirius red staining

The liver histology sections were dewaxed in xylene and rehydrated in diminishing concentrations of ethanol. The staining buffer was freshly prepared according to the manufacturer's instruction (Sbjbio, China). Briefly, the sections were incubated with the Sirius red staining solution for 1 h at room temperature. After washed with PBS, the sections were stained with Mayer hematoxylin solution for the nucleus. The stained histology sections were then photographed using an Olympus BX51 phase contrast light microscope. The percentage of Sirius red positive areas were analyzed using ImageJ program.

Nile red staining

The Primary osteoblasts and primary osteoclasts were fixed with 4% PFA after cells were treated with recombinant LCAT and then stained with DAPI and (Sigma-Aldrich) for 2 h at 37°C. The final concentration of Nile Red dye was 0.1 μg/mL. After washed with PBS twice, the stained histology slides were photographed using Olympus FV3000 confocal microscope to analyze the intracellular cholesterol level.

Filipin III staining

The primary osteoblasts and primary osteoclasts were treated with 100 ng/mL rLCAT and 10 mM HP-β-CD for 48 h. The cells were fixed by 4% PFA for 10 min and then incubated with 10 μg/mL Filipin III (Sigma-Aldrich) solution for 2 h. After washed with PBS, the cells were visualized by Olympus FV3000 confocal microscope, with excitation at 340-380 nm and emission at 385-470 nm.

Calcein staining and analysis

Calcein was used to label the front of newly formed bone to enable longitudinal bone mineral appositional rates. The mice were injected with calcein (Sigma-Aldrich) at a dosage of 15 mg/kg at 9 and 2 days prior to mice sacrifice. The right femurs were fixed with 4% PFA, and were cut into 15 μm sections using a hard-tissue microtome (EXAKT, Germany). The histology slides were analyzed and photographed using Olympus FV3000 confocal microscope and the bone mineral appositional rates (MAR) were calculated as the distance of two calcein labels divided by the time interval between two injections.

Co-immunoprecipitation assay

Co-immunoprecipitation (Co-IP) assay was performed to analyze the binding between PP2Acα and USF1. Briefly, proteins of the primary hepatocytes or liver tissues were extracted according to the previous protocol (Dandri et al., 2001). And the total protein concentrations were evaluated using the BCA protein assay kit. The mouse anti-PP2Acα and anti-USF1 antibody or a control mouse IgG was used for immunoprecipitation and incubated for overnight at 4°C to form the immune complex. The Pierce protein A/G Magnetic beads of CO-IP kit were washed twice with ice-cold IP lysis/Wash buffer. The antigen sample mixture was then added to the tube containing the pre-washed magnetic beads and incubated at room temperature for 1 h with mixing. After washing the beads three times, the eluted proteins were subjected to SDS-PAGE and western-blot analysis with anti-PP2Acα and anti-USF1 antibodies.

Cholesterol transplantation and *in vivo* imaging analysis

For detection the role of LCAT in transport cholesterol back to liver, the cholesterol transplantation was detected and analyzed by the *in vivo* imaging system (IVIS) in nude mice bought from. After anesthetized by isoflurane, the skin of right femur was cut up and 100 μg NBD-cholesterol (Invitrogen) was injected into the bone marrow. 0, 6, 24 and 48 h later, the mice were anesthetized and imaged by the IVIS using sequential 30 s exposure for 12 min.

Dual luciferase reporter assay

For detection the impact of p-USF1 on the LCAT transcriptional activity, the murine liver cell line AML12 cells were plated in 12-well culture plates and transfected with the pcDNA 3.1-*Usf1* plasmid and the luciferase reporter of pGL4.10-*Lcat* promoter construct using Lipofectamine 2000 according to manufacturer's instructions (Invitrogen). 24 h post-transfection, cells were then transfected with or without the *siPP2Acα* using Lipofectamine 2000. After incubated for additional 36 h, the CCl_4 (1 μM) was added into the cells for incubation for another 12 h. The luciferase activity was measured and normalized against Renilla luciferase activity as an internal control (Promega) in GloMaxTM 96 Microplate Luminometer. The similar protocol was also carried out to detect the effect of the T153A mutant USF-1 (pcDNA3.1-*mUsf1*) on the *Lcat* transcriptional activity under the condition of *PP2Acα* deficiency.

QUANTIFICATION AND STATISTICAL ANALYSIS

Statistical analyses were performed using GraphPad Prim 8.0 software. All data are shown as the mean ± SEM and a P value < 0.05 with two-tailed test was considered as significant. For differences between 2 groups, unpaired t test was used. For analyzing data of > 2 groups, statistical methods of One-way or Two-way ANOVA with Tukey's multiple comparison test were used. For analyzing the stages of hepatic fibrosis of patients, rank sum test was used. Correlations were assessed using Spearman's rank correlation test. Statistical parameters are noted in the figure legends. All experiments were performed and analyzed using 3 individual samples, unless otherwise mentioned. All the mice were assigned to groups randomly, the experiments were done in a blinded fashion. The sample sizes of individuals with hepatic hemangioma, cirrhosis and HOD were determined by power analysis with PASS 15.0 software. The sample sizes of animal experiments were not determined by any analysis. A total of 25 individuals were recruited and finally 16 individuals were enrolled in the study.